LETTER

https://doi.org/10.1038/s41586-019-1519-2

Structure and mechanism of mitochondrial proton–translocating transhydrogenase

Domen Kampjut[1] & Leonid A. Sazanov[1]*

Proton-translocating transhydrogenase (also known as nicotinamide nucleotide transhydrogenase (NNT)) is found in the plasma membranes of bacteria and the inner mitochondrial membranes of eukaryotes. NNT catalyses the transfer of a hydride between NADH and $NADP^+$, coupled to the translocation of one proton across the membrane. Its main physiological function is the generation of NADPH, which is a substrate in anabolic reactions and a regulator of oxidative status; however, NNT may also fine-tune the Krebs cycle[1,2]. NNT deficiency causes familial glucocorticoid deficiency in humans and metabolic abnormalities in mice, similar to those observed in type II diabetes[3,4]. The catalytic mechanism of NNT has been proposed to involve a rotation of around 180° of the entire NADP(H)-binding domain that alternately participates in hydride transfer and proton-channel gating. However, owing to the lack of high-resolution structures of intact NNT, the details of this process remain unclear[5,6]. Here we present the cryo-electron microscopy structure of intact mammalian NNT in different conformational states. We show how the NADP(H)-binding domain opens the proton channel to the opposite sides of the membrane, and we provide structures of these two states. We also describe the catalytically important interfaces and linkers between the membrane and the soluble domains and their roles in nucleotide exchange. These structures enable us to propose a revised mechanism for a coupling process in NNT that is consistent with a large body of previous biochemical work. Our results are relevant to the development of currently unavailable NNT inhibitors, which may have therapeutic potential in ischaemia reperfusion injury, metabolic syndrome and some cancers[7–9].

Transhydrogenase always exists as a homodimer. Each monomer is composed of three domains—NAD(H)-binding dI, transmembrane dII and NADP(H)-binding dIII—which are split between one, two or three polypeptides (Fig. 1a, Extended Data Fig. 1). The structures of isolated domains and the heterotrimeric dI_2dIII complex (dimeric dI bound to a single dIII) from several species have been solved in native, reduced or oxidized states; however, these structures do not explain the unique mechanism of NNT, which requires coordination of all the domains in the dimer[10–14]. The only structure so far that has shown the intact architecture of NNT was determined at low resolution (6.9 Å) for the *Thermus thermophilus* enzyme[5] in the presence of $NADP^+$. The structure from *T. thermophilus* showed that NNT is an asymmetric dimer in which one dIII is 'face-up' (presenting NADP(H) to dI for hydride transfer) and the other dIII is 'face-down' (with the NADP(H)-binding site facing dII)[5] (Fig. 1b). This led to a proposal of a 'division of labour' mechanism, in which dIII rotates approximately 180° and functions alternately in proton translocation (face-down) and hydride transfer (face-up)[6]. Although this mechanism is consistent with the architecture of NNT that was observed in *T. thermophilus*, and is consistent with most previous biochemical work, in the absence of detailed structural information it was largely speculative. Furthermore, the proposed mechanism also failed to account for the different effects of $NADP^+$ and NADPH on the conformation of NNT[15,16].

To define the mechanism, we solved the structures of a stable and active preparation of ovine NNT at pH 7.4 in the apo, $NADP^+$-bound and NADPH-bound forms at up to 2.9 Å resolution using cryo-electron microscopy (cryo-EM) (Extended Data Figs. 2–4). Using the electron microscopy maps, we were able to produce high-quality, full atomic models of mammalian NNT (Extended Data Figs. 5, 6, Extended Data Table 1). The only observed three-dimensional (3D) class of particles in the apo-NNT dataset adopted an unexpected 'double face-down' conformation, in which both dIII domains are tightly attached to dII in the face-down orientation (Fig. 1a). In the $NADP^+$-bound NNT dataset the main class showed a similar double face-down conformation, but with improved resolution—possibly due to the stabilizing effects of the bound nucleotide (Figs. 1c, 2a, Extended Data Figs. 3, 5). A second, less-populated class of particles in the $NADP^+$-bound NNT dataset adopted a 'single face-down' conformation (Fig. 1b), in which one dIII is detached from dII, dI_2 is more tilted and, notably, the proton channel has different conformations in the two monomers, as discussed below (Extended Data Fig. 6). Incubating NNT with NADPH induced global conformational changes, as predicted[15,16], and we did not observe any particles of the double face-down class (Fig. 2a, Extended Data Fig. 4a). Only around 11% of particles had one dIII weakly bound to dII, and the rest of the particles corresponded to many different 'double-detached' classes. In the double-detached conformation, both dIII domains are detached and tethered only by a dII–dIII linker, allowing the tilting of dI_2 in all directions (Fig. 2). We conclude that in the mammalian enzyme, $NADP^+$ and NADPH on their own promote the detaching of dIII to various degrees, but do not lead to the formation of a stable dI–dIII (face-up) interface.

The mammalian-specific transmembrane (TM) helices TM1 and TM5 form an extended interface of the dII dimer, which might stabilize mammalian NNT together with the dI–dII linker described (along with some other novel features of the structure) in the Supplementary Discussion (Fig. 3a). The core fold of dII is conserved between *T. thermophilus* and ovine NNT. The probable proton translocation pathway, as proposed in previous studies, is formed by TM3–TM4, TM9–TM10 and TM13–TM14, arranged in a hexagram[5,17,18]. We observed two conformations of the proton channel depending on the attachment of the dIII domain, which inserts its helix 4 (residues 929–937) and the $NADP^+$-coordinating loop (residues 920–927) deeply between the key transmembrane helices TM3, TM9 and TM13, pushing them apart (Fig. 4a, b). Analysis of the proton channel in the dIII-attached state starting from the negatively charged side (N side) of the membrane (that is, the bacterial cytoplasm or mitochondrial matrix) indicates a narrow block followed by a group of conserved polar residues (H664, N796 and N489), a dry hydrophobic stretch and a cluster of negatively charged residues at the exit—appropriate for proton 'gathering' from the positively charged side (P side) in the forward reaction (Fig. 3b, c, Extended Data Fig. 6g). Notably, the secondary structures of helices TM3 and TM9 are strongly distorted around this region, which suggests that conformational flexibility is required for the proton translocation (Fig. 3b).

[1]Institute of Science and Technology Austria, Klosterneuburg, Austria. *e-mail: sazanov@ist.ac.at

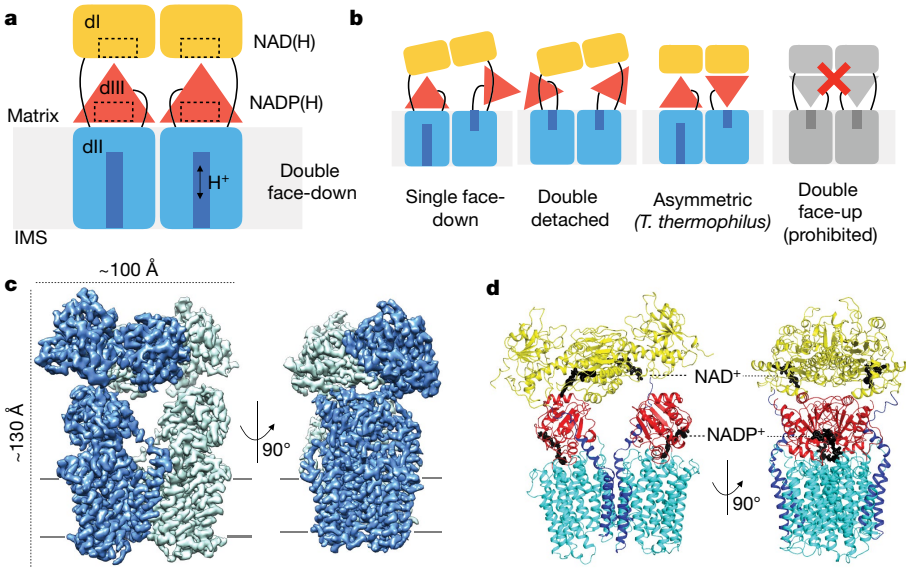

Fig. 1 | Mammalian transhydrogenase. **a**, Schematic representation of the domains, linkers, binding sites and conformation of the mammalian transhydrogenase in the double face-down (both dIII attached to dII) conformation (apo and $NADP^+$ datasets). IMS, intermembrane space. **b**, Other conformations of NNT present in our datasets: one dIII detached (single face-down) or both dIIIs detached (double detached) in the presence of $NADP^+$ and NADPH, the asymmetric conformation in *T. thermophilus* (note the absence of a dI–dII linker) and the sterically prohibited double-face-up conformation. **c**, The cryo-EM density of transhydrogenase in the double face-down $NADP^+$ state, with the two monomers coloured differently. **d**, Atomic model of mammalian NNT, with the domains coloured as in **a** and the mammalian-specific elements (dI–dII linker, TM1 and TM5) highlighted in blue. Bound nucleotides are shown in black.

The detaching of dIII from dII induces a substantial shift of the cytoplasmic (matrix-facing) loops CL6 and CL7, helix CL8 and the matrix-facing sides of TM9–TM11, TM13 and TM14 towards the centre of dII, with displacements of up to 3.5 Å (Fig. 4a). This results in a more compact packing of the helices and renders dII in the dIII-detached state much more similar to dII from *T. thermophilus* (which is also detached from dIII) than is dII in the dIII-attached state (Extended Data Fig. 7a, b). With dIII detached, the proton channel adopts a more closed conformation from the P side (Extended Data Fig. 7f, g). Notably, the key residue H664 (suggested to be involved in proton translocation[18]) and S799 both flip down (towards the P side)—in line with the predictions of molecular dynamics for the serine homologue[17] (Fig. 4a, Extended Data Fig. 7c). H664 becomes more accessible for protonation from the matrix side, owing to both the rearrangements in the channel and, notably, the removal of the whole dIII acting as a 'plug', which exposes the dII surface to the solvent (Fig. 3). Modelling of

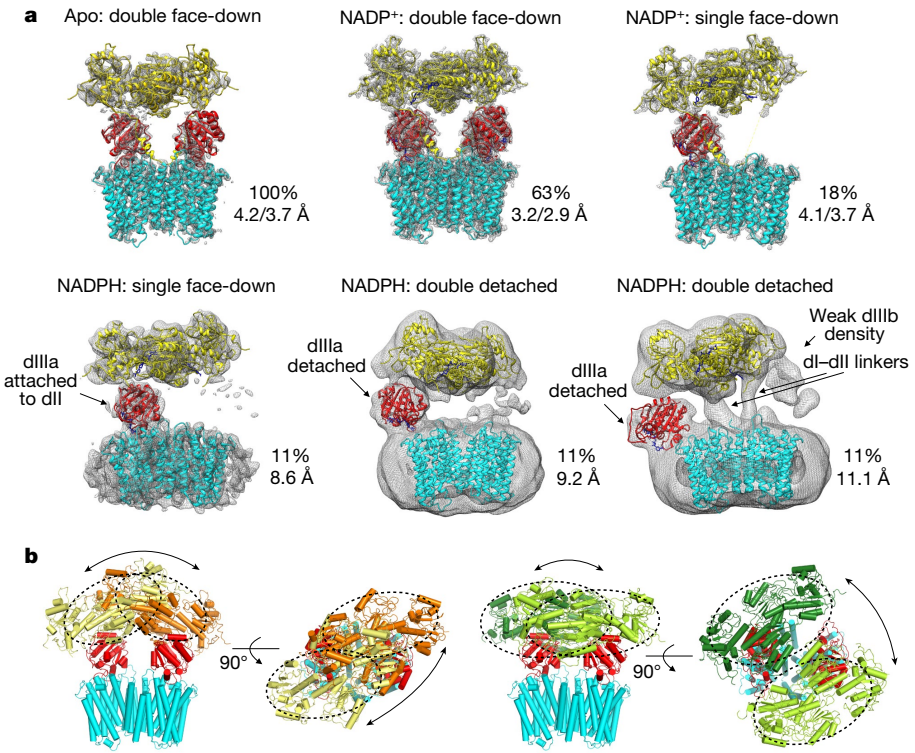

Fig. 2 | NADP(H) binding influences the overall conformation of transhydrogenase. a, Structures and relative abundances of different conformations of NNT observed in the datasets. The double face-down conformation was the only form observed in apo-NNT and was the major form in the $NADP^+$ datasets; the single face-down (or one dIII detached) conformation was a minor form in $NADP^+$ and NADPH datasets, and the double-detached (both dIIIs detached) conformation was a major form in the NADPH dataset. **b**, NNT–NADPH particles were analysed using multibody refinement in RELION 3.0 using dI_2 and dII_2 masks. This revealed a high degree of tilting of the dI_2 domain in all directions, which is consistent with both dIII being dissociated from the rest of the particle and disrupting the overall solidity of the enzyme. Two bins of particles from the extreme ends of the distribution along two principal components are aligned by dII_2 and the difference in dI_2 tilt is depicted in different shades of yellow and green.

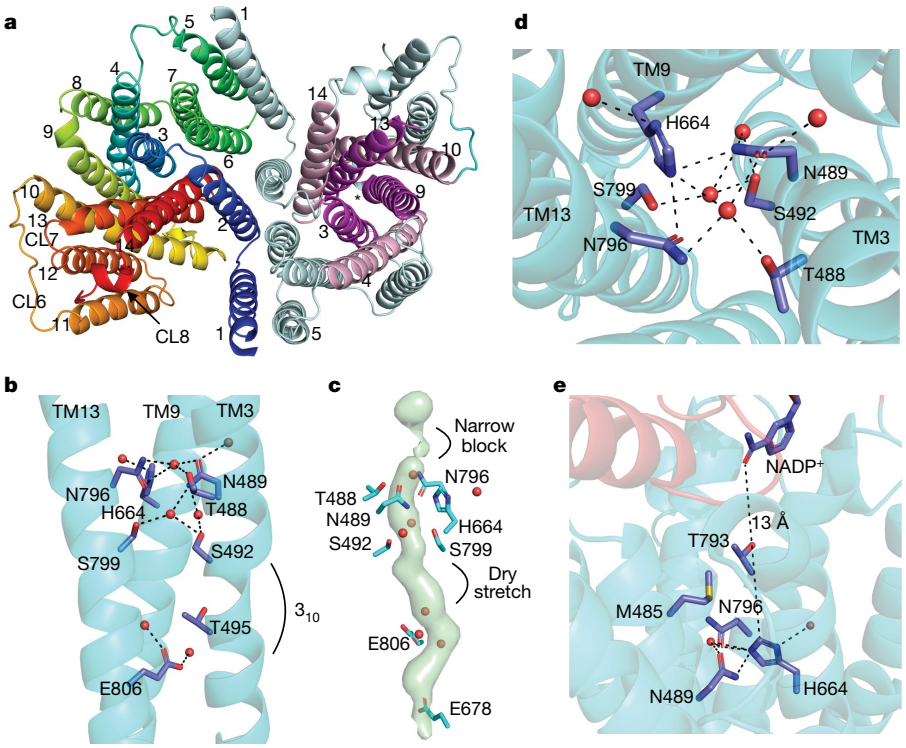

Fig. 3 | The transmembrane dII domain and the proton translocation pathway in the double face-down conformation. **a**, Organisation of transmembrane helices in the NNT dimer. The monomer on the left is coloured blue to red from the N to the C termini; for the monomer on the right, the inner proton channel-lining TM helices are highlighted in magenta with the outer scaffolding helices in pink. The dimer interface consisting of eight helices is considerably larger than the four-helix interface of *T. thermophilus*. **b**, Conserved residues of the proton transfer pathway. Dowser-predicted water molecules are shown as red spheres. The distorted α-helical area is indicated as the 3_{10} helix. **c**, The proton translocating pore features a narrow block close to the matrix (N) side and a dry stretch in the middle of the membrane. Four of the predicted water molecules lie within the central pore. **d**, Detailed view of the matrix proton-entry site, with conserved residues and hydrogen-bonding network shown. **e**, The nicotinamide ring is bound 13 Å away from H664, which allows for electrostatic interactions between them.

water molecules is consistent with this conclusion: in dIII-attached dII, one water molecule is bound above and one below the H664–N489–N796 ring, whereas in the dIII-detached state, the P side water molecule disappears and the S799 flips downwards (Extended Data Fig. 7d). Cryo-EM density of the highly coordinated P side water molecule is visible in our 2.9 Å map (Extended Data Fig. 7e).

The conformation of dIII bound to dII differs from crystal structures of isolated dIII at the interface-forming sites and in the nucleotide-binding pocket[10,11,14] (Fig. 4b, Extended Data Fig. 8a). Loop E (residues 1002–1010) is a transhydrogenase-specific element that occludes the nucleotide in isolated dIII, preventing its exchange with the solution[10,12]. In our double face-down NADP$^+$-bound NNT structure, this loop is displaced by CL7 from dII and has only very weak density, which allows NADP$^+$ to insert deeply into the proton channel. In the apo-NNT structure, loop E is completely disordered, and this enables free exchange of nucleotides (Extended Data Fig. 8b, c). The binding of dII also induces the structure to open around the ribose diphosphate—through the breaking of the R925–Y890 stacking interactions and the R925 bonds with the diphosphate—which has not previously been observed in any dIII or dI$_2$dIII crystal structures[10,12]

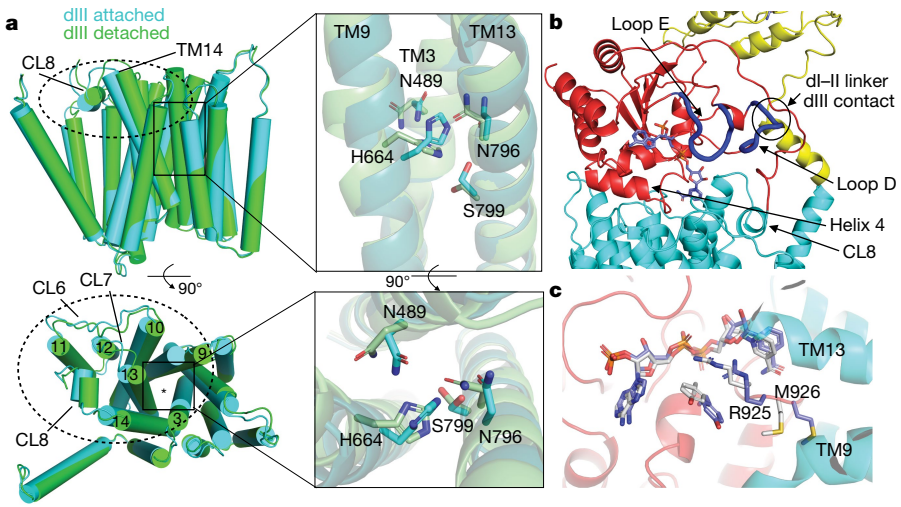

Fig. 4 | Attachment of dIII changes the conformation of the proton translocation pathway and opens the NADP(H)-binding pocket. **a**, Comparison of dII in dIII-associated (cyan) and dIII-dissociated (green) states from the single face-down structure. dIII dissociation results in the tilting of TM helices towards the central axis. The magnified views show rearrangement of the N side proton-entry side in dII. Notably, H664 and S799 flip and the surrounding N489 and N796 residues undergo a substantial change in conformation, opening the channel to the N side when dIII is detached. **b**, The interface between dIII and dII. Helix 4 and loop D, which are conserved transhydrogenase-specific elements flanking the central Rossmann fold, form extensive contacts with the cytoplasmic loops of the dII. Loop E is displaced by dII binding. **c**, Comparison of the NADP(H) binding pockets of ovine dIII–dII and human dIII–NADP$^+$ (Protein Data Bank (PDB): 1DJL, in grey) reveals the breaking of the interactions between R925 and diphosphate and between R925 and Y890.

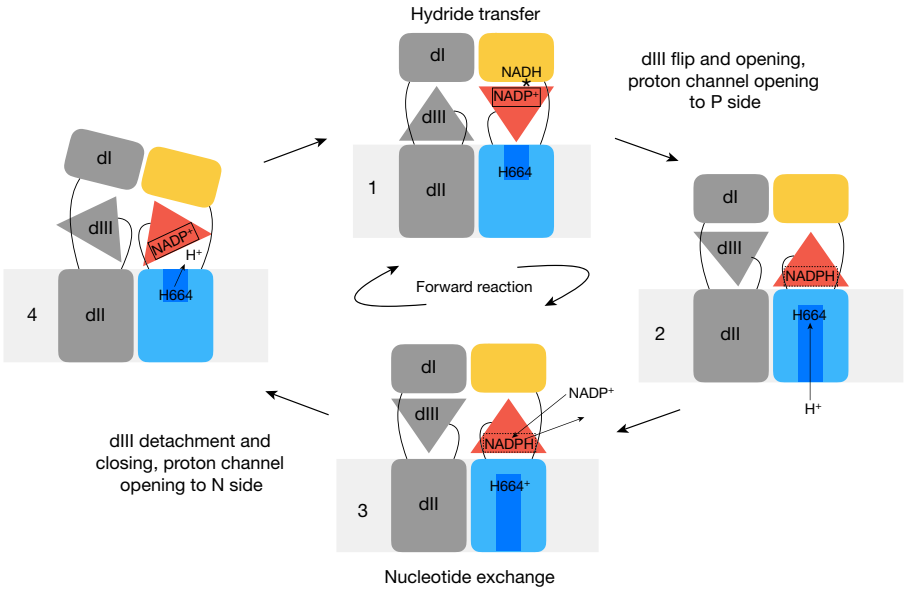

Fig. 5 | The catalytic mechanism of transhydrogenase. NNT always operates as a dimer. Key steps in the mechanism for the coloured monomer are described in the main text. The other monomer (shown in grey) operates in the anti-phase fashion. The nucleotide in dIII exists in either an occluded state (full line) or an open state (dashed line). Asterisk in step 1 indicates hydride transfer. The key checkpoint in the mechanism is that proton translocation across the membrane cannot proceed to completion without nucleotide exchange (step 3). The interactions between dIII–NADP(H) and dII–H664 that ensure that this coupled reaction can be summarized as follows: $NADP^+$ interacts strongly with H664 but repels $H664^+$, whereas NADPH interacts strongly with $H664^+$ and repels H664.

(Fig. 4c). In apo-NNT, R925 is rotated outwards, which makes this opening up of the structure even more pronounced (Extended Data Fig. 8c). We conclude that the $NADP^+$ molecule is partially occluded in the binding site in the face-down dIII, but less so than in the detached dIII.

We now propose a revised catalytic mechanism for transhydrogenase, on the basis of our observations as well as previous functional and mutagenesis results (Extended Data Fig. 9a, Supplementary Tables 1–3). The proposed mechanism involves dIII flipping, as has been suggested previously[6], and the main considerations are stated below.

From previous work, the following features have been well established: first, dI remains open to nucleotide exchange throughout the reaction cycle, as confirmed by the high rates of binding of NAD(H) to dI during the catalytic cycle[19,20]. Second, the dI–dIII interface is transient, hydride transfer is fast and it does not limit the reaction[21]. Third, when dIII is detached, bound NADP(H) is occluded; this is evidenced by a decreased dissociation constant (K_d) for NADP(H) in isolated dIII (around 10^{-9} M) compared to the intact enzyme (around 10^{-6} M), the co-purification of the bound nucleotide when dIII is isolated, and the observation of a well-ordered and closed loop E in structures of isolated dIII[10,12,22,23]. Mutations of H664 and R544 that lead to the detachment of dIII also result in its co-purification with NADP(H)[18,24].

The following principle had been speculatively proposed in a previous study[6], and is now validated by our structures: the formation of the dII–dIII interface is necessary for nucleotide exchange, as shown by our structures that demonstrate the opening of loop E (Extended Data Fig. 8). This principle is further validated by R544 mutants, which disrupt the dII–dIII interface[24].

Insights from the structural data presented here are as follows. First, apo-dIII is attached to dII, and can detach only when bound to NADP(H) (Fig. 2a). Second, the proton channel is open only to the N side when dIII is detached and only to the P side when dIII is attached (Fig. 4, Extended Data Fig. 7). Third, the detachment of dIII–NADP(H) from dII depends on the protonation state of the key histidine in the proton channel (H664 in ovine NTT): dIII–$NADP^+$ is detached from protonated $H664^+$ but is attached to the neutral H664. Conversely, dIII–NADPH is detached from H664 and is attached to $H664^+$. In other words, the attachment of dIII–NADP(H) modifies the pK_a of H664: bound NADPH promotes its protonation and $NADP^+$ promotes its deprotonation. This is consistent with direct electrostatic interaction between H664 and the charged nicotinamide ring (positive in $NADP^+$ and negative in NADPH); they are separated by only about 13 Å (Fig. 3e), which is much closer than the 19 Å separation that had been predicted previously[5]. The pK_a of H664 has been experimentally estimated at around 5.5[25]; this is consistent with PROPKA calculations on our structures, which suggest that the pK_a is around 5. Because our datasets were collected at pH 7.4—when H664 is mostly deprotonated—we observed that dIII–$NADP^+$ was mostly attached and that dIII–NADPH was mostly detached, which is consistent with this proposal. The detachment of dIII from dII in the presence of $NADP^+$ and $H664^+$ is also validated by the observation that the rate of $NADP^+$-dependent cyclic reaction (hydride transfer from NADH to NAD^+ via occluded $NADP^+$) is increased at low pH values[25,26]. The cyclic reaction cannot provide information on the specific effects of NADPH, because the main species in the NADPH-initiated cycle[26] is still the occluded dIII–$NADP^+$. However, the NADPH-stimulated detachment of dIII at neutral or higher pH values has been demonstrated experimentally[15] by stimulated trypsinolysis in the presence of NADPH, but not $NADP^+$ or NAD(H). We analysed the full pH dependence of trypsinolysis in the presence of all substrates and found that, when the pH is greater than 6, NADPH stimulates trypsinolysis more than does $NADP^+$; conversely, $NADP^+$ has the larger stimulating effect at pH values below 6 (Extended Data Fig. 2e). These findings validate the predicted interactions between H664 and NADP(H).

On the basis of these principles we propose a robust mechanism that explains the full reversibility of NNT, the pH dependencies of the reverse and cyclic reactions, and the effects of $NADP^+$ and NADPH on the conformation of NNT (Fig. 5, Supplementary Video 1). This mechanism is validated by the phenotypes of various mutants—particularly within the proton translocation pathway, the E loop and the dII–dIII interface (Supplementary Tables 1–3). Proton translocation and nucleotide exchange are tightly coupled by direct interactions between H664 and NADP(H): the attachment and detachment of NADP(H)-bound dIII is strictly dependent on the protonation state of H664 and opens the proton channel to the opposite sides of the membrane. 'Slipping', or uncoupling, is prevented because proton translocation cannot happen without nucleotide exchange. The forward reaction occurs under a high proton motive force and an excess of $NADP^+$. When dIII is not

attached, H664 is unprotonated because it is exposed to the matrix, which has a relatively high pH (step 1, Fig. 5). After hydride transfer, dIII–NADPH swivels down and attaches to dII-H664, opening it to the P side (step 2). This enables the protonation of H664 from the P side, where the pH is lower (and the pK_a of the histidine is increased, owing to its interaction with NADPH). Nucleotide exchange then follows, owing to an excess of $NADP^+$ and the opened dIII (step 3). dIII–$NADP^+$ detaches from dII-$H664^+$; this opens dII to the N side where $H664^+$ is deprotonated (step 4). dIII–$NADP^+$ then associates with dI, allowing for hydride transfer (return to step 1). All the steps can be easily reversed in the appropriate conditions—high concentration of NADPH and a low proton motive force—giving rise to the reverse reaction (Extended Data Fig. 9b, Supplementary Discussion).

This mechanism suggests the anti-phase action of two monomers—a 'division of labour', as has been suggested previously[6]. This is essential for those bacterial enzymes that lack a dI–dII linker, because one dIII must be attached to dI_2 at all times to prevent the loss of dI_2. Mammalian NNT also shows half-of-sites inhibition, a catalytically inactive monomeric dI, and negative cooperativity of NAD(H) and NADP(H) sites between monomers, all of which strongly suggest an anti-phase mechanism[27–29]. The presence of the dI–dII linker could render the strict anti-phase action less of a requirement for the mammalian enzyme; however, anti-phase action avoids steric clashes between dIIIs (which would happen if they were independently functioning), and the swivelling 'up' of one dIII is the best explanation for the initiation of the detachment—after hydride transfer—of the other dIII from dI_2. The dI–dII linker could also contribute towards the higher efficiency of the mammalian enzyme compared with its bacterial counterpart: a weaker dI–dIII interface could enable faster turnover of the mammalian enzyme. Indeed, biochemical data confirm that the dI–dIII interaction in bacterial enzymes is much stronger than in mammalian analogues[20,30]. The existence of a unique auto-inhibited double face-down conformation in mammalian NNT could be an important additional aspect of its regulation. Further data will be required to determine the importance of the anti-phase action in NNT, as well as to assess all the implications of the proposed mechanism.

Online content

Any methods, additional references, Nature Research reporting summaries, source data, extended data, supplementary information, acknowledgements, peer review information; details of author contributions and competing interests; and statements of data and code availability are available at https://doi.org/10.1038/s41586-019-1519-2.

Received: 5 February 2019; Accepted: 31 July 2019;
Published online 28 August 2019.

1. Jackson, J. B. A review of the binding-change mechanism for proton-translocating transhydrogenase. *Biochim. Biophys. Acta.* **1817**, 1839–1846 (2012).
2. Sazanov, L. A. & Jackson, J. B. Proton-translocating transhydrogenase and NAD- and NADP-linked isocitrate dehydrogenases operate in a substrate cycle which contributes to fine regulation of the tricarboxylic acid cycle activity in mitochondria. *FEBS Lett.* **344**, 109–116 (1994).
3. Meimaridou, E. et al. Mutations in NNT encoding nicotinamide nucleotide transhydrogenase cause familial glucocorticoid deficiency. *Nat. Genet.* **44**, 740–742 (2012).
4. Toye, A. A. et al. A genetic and physiological study of impaired glucose homeostasis control in C57BL/6J mice. *Diabetologia* **48**, 675–686 (2005).
5. Leung, J. H. et al. Division of labor in transhydrogenase by alternating proton translocation and hydride transfer. *Science* **347**, 178–181 (2015).
6. Jackson, J. B., Leung, J. H., Stout, C. D., Schurig-Briccio, L. A. & Gennis, R. B. Review and Hypothesis. New insights into the reaction mechanism of transhydrogenase: Swivelling the dIII component may gate the proton channel. *FEBS Lett.* **589**, 2027–2033 (2015).
7. Li, S. et al. Nicotinamide nucleotide transhydrogenase-mediated redox homeostasis promotes tumor growth and metastasis in gastric cancer. *Redox Biol.* **18**, 246–255 (2018).
8. Santos, L. R. B. et al. NNT reverse mode of operation mediates glucose control of mitochondrial NADPH and glutathione redox state in mouse pancreatic β-cells. *Mol. Metab.* **6**, 535–547 (2017).
9. Nickel, A. G. et al. Reversal of mitochondrial transhydrogenase causes oxidative stress in heart failure. *Cell Metab.* **22**, 472–484 (2015).
10. Prasad, G. S., Sridhar, V., Yamaguchi, M., Hatefi, Y. & Stout, C. D. Crystal structure of transhydrogenase domain III at 1.2 Å resolution. *Nat. Struct. Biol.* **6**, 1126–1131 (1999).
11. Cotton, N. P. J., White, S. A., Peake, S. J., McSweeney, S. & Jackson, J. B. The crystal structure of an asymmetric complex of the two nucleotide binding components of proton-translocating transhydrogenase. *Structure* **9**, 165–176 (2001).
12. Sundaresan, V., Yamaguchi, M., Chartron, J. & Stout, C. D. Conformational change in the NADP(H) binding domain of transhydrogenase defines four states. *Biochemistry* **42**, 12143–12153 (2003).
13. Johansson, T. et al. X-ray structure of domain I of the proton-pumping membrane protein transhydrogenase from *Escherichia coli*. *J. Mol. Biol.* **352**, 299–312 (2005).
14. Mather, O. C., Singh, A., van Boxel, G. I., White, S. A. & Jackson, J. B. Active-site conformational changes associated with hydride transfer in proton-translocating transhydrogenase. *Biochemistry* **43**, 10952–10964 (2004).
15. Yamaguchi, M., Wakabayashi, S. & Hatefi, Y. Mitochondrial energy-linked nicotinamide nucleotide transhydrogenase: effect of substrates on the sensitivity of the enzyme to trypsin and identification of tryptic cleavage sites. *Biochemistry* **29**, 4136–4143 (1990).
16. Yamaguchi, M. & Hatefi, Y. Mitochondrial nicotinamide nucleotide transhydrogenase: NADPH binding increases and NADP binding decreases the acidity and susceptibility to modification of cysteine-893. *Biochemistry* **28**, 6050–6056 (1989).
17. Padayatti, P. S. et al. Critical role of water molecules in proton translocation by the membrane-bound transhydrogenase. *Structure* **25**, 1111–1119 (2017).
18. Glavas, N. A., Hou, C. & Bragg, P. D. Involvement of histidine-91 of the β subunit in proton translocation by the pyridine nucleotide transhydrogenase of *Escherichia coli*. *Biochemistry* **34**, 7694–7702 (1995).
19. Venning, J. D., Peake, S. J., Quirk, P. G. & Jackson, J. B. Stopped-flow reaction kinetics of recombinant components of proton-translocating transhydrogenase with physiological nucleotides. *J. Biol. Chem.* **275**, 19490–19497 (2000).
20. Yamaguchi, M. & Hatefi, Y. High cyclic transhydrogenase activity catalyzed by expressed and reconstituted nucleotide-binding domains of *Rhodospirillum rubrum* transhydrogenase. *Biochim. Biophys. Acta* **1318**, 225–234 (1997).
21. Venning, J. D., Bizouarn, T., Cotton, N. P. J., Quirk, P. G. & Jackson, J. B. Stopped-flow kinetics of hydride transfer between nucleotides by recombinant domains of proton-translocating transhydrogenase. *Eur. J. Biochem.* **257**, 202–209 (1998).
22. Fjellström, O., Johansson, C. & Rydström, J. Structural and catalytic properties of the expressed and purified NAD(H)- and NADP(H)-binding domains of proton-pumping transhydrogenase from *Escherichia coli*. *Biochemistry* **36**, 11331–11341 (1997).
23. Bizouarn, T., van Boxel, G. I., Bhakta, T. & Jackson, J. B. Nucleotide binding affinities of the intact proton-translocating transhydrogenase from *Escherichia coli*. *Biochim. Biophys. Acta* **1708**, 404–410 (2005).
24. Glavas, N. A. & Bragg, P. D. The mechanism of hydride transfer between NADH and 3-acetylpyridine adenine dinucleotide by the pyridine nucleotide transhydrogenase of *Escherichia coli*. *Biochim. Biophys. Acta* **1231**, 297–303 (1995).
25. Sazanov, L. A. & Jackson, J. B. Cyclic reactions catalysed by detergent-dispersed and reconstituted transhydrogenase from beef-heart mitochondria; implications for the mechanism of proton translocation. *Biochim. Biophys. Acta* **1231**, 304–312 (1995).
26. Hutton, M., Day, J. M., Bizouarn, T. & Jackson, J. B. Kinetic resolution of the reaction catalysed by proton-translocating transhydrogenase from *Escherichia coli* as revealed by experiments with analogues of the nucleotide substrates. *Eur. J. Biochem.* **219**, 1041–1051 (1994).
27. Phelps, D. C. & Hatefi, Y. Interaction of purified nicotinamidenucleotide transhydrogenase with dicyclohexylcarbodiimide. *Biochemistry* **23**, 4475–4480 (1984).
28. Yamaguchi, M. & Hatefi, Y. Energy-transducing nicotinamide nucleotide transhydrogenase. Nucleotide binding properties of the purified enzyme and proteolytic fragments. *J. Biol. Chem.* **268**, 17871–17877 (1993).
29. Obiozo, U. M. et al. Substitution of tyrosine 146 in the dI component of proton-translocating transhydrogenase leads to reversible dissociation of the active dimer into inactive monomers. *J. Biol. Chem.* **282**, 36434–36443 (2007).
30. Fjellström, O. et al. Catalytic properties of hybrid complexes of the NAD(H)-binding and NADP(H)-binding domains of the proton-translocating transhydrogenases from *Escherichia coli* and *Rhodospirillum rubrum*. *Biochemistry* **38**, 415–422 (1999).

METHODS

Purification of transhydrogenase from ovine mitochondria. All procedures described were carried out at 4 °C. Mitochondria were purified from fresh ovine heart tissue by differential centrifugation and stored at −80 °C according to procedure 3 from ref. [31]. On the day of purification, inner mitochondrial membranes were isolated as described for the purification of respiratory complex I[32]. In brief, mitochondria (10 g) were ruptured by homogenization in 100 ml Milli-Q water, then membranes were separated by centrifugation at 50,000*g* for 45 min and resuspended in 100 ml of buffer M (20 mM HEPES, pH 7.4, 40 mM NaCl, 1 mM EDTA, 10% v/v glycerol, 2 mM DTT, 0.002% PMSF). After another round of resuspension and centrifugation, membranes were resuspended in 50 ml of buffer M. Lauryl maltose neopentyl glycol (LMNG; 10%) was added dropwise to this suspension to 1% and, after stirring for 45 min, the sample was centrifuged at 50,000*g* for 45 min. The supernatant was filtered with a 0.22-μm filter and loaded onto a 45-ml Q-Sepharose HP anion-exchange column equilibrated in buffer Q-A (20 mM HEPES pH 7.4, 40 mM NaCl, 2 mM EDTA, 10% v/v glycerol, 1 mM DTT, 0.05% LMNG). Proteins were eluted with a 400 ml linear gradient with 0–17% Q-B buffer (Q-A buffer with 1 M NaCl). NNT eluted as a broad peak at around 110 mM NaCl and fractions containing substantial amounts of NNT (based on the activity assay and the SDS–PAGE profile) were pooled and dialysed overnight against a tenfold volume excess of buffer D (20 mM MES, pH 5.8, 2 mM EDTA, 10% v/v glycerol, 1 mM DTT, 0.01% LMNG). This lowered the pH of the sample below 6 and the conductance below 2 mS cm^{-1}, and made it suitable for loading onto a 45 ml SP-Sepharose HP cation-exchange column equilibrated in buffer SP-A (20 mM MES pH 5.8, 10 mM NaCl, 2 mM EDTA, 10% v/v glycerol, 1 mM DTT, 0.025% LMNG). Elution with a 100 ml 0–20% linear gradient with buffer SP-B (SP-A with 1 M NaCl) gave a sharp elution peak of relatively pure NNT at around 35 mM NaCl (conductance 4 mS cm^{-1}). Fractions containing NNT were concentrated to 4 mg ml^{-1} using a 100-kDa cut-off concentrator and stored at 30% glycerol under liquid nitrogen. On the day of a cryo-EM grid preparation, a sample of NNT was thawed on ice and loaded onto a Superose 12 10/300 gel filtration column equilibrated in buffer GF (20 mM HEPES, pH 7.4, 50 mM NaCl, 1 mM EDTA, 0.002% LMNG) to remove excess detergent and remaining protein contaminants. The purest and the most concentrated fractions of NNT eluted at around 10.5 ml, and were concentrated to 5 mg ml^{-1} using a Millipore 100-kDa cut-off filter and used immediately for cryo-EM grid preparation (Extended Data Fig. 2). In some purifications 0.002% LMNG in GF buffer was substituted by 0.05% fluorinated octyl maltoside (FOM), which gave a monodisperse and highly active NNT; however, grids suitable for cryo-EM data collection could not be prepared from FOM preparations because the protein started to aggregate on the grid at concentrations higher than 2 mg ml^{-1}. The apo form of our preparation lacked any bound nucleotide, as confirmed by the absence of a cyclic reaction without the addition of exogenous $NADP^+$ (data not shown).

Electron microscopy. 0.05% CHAPS was added to the protein sample before grid preparation to improve the quality of the ice and the particle distribution. Substrates at 5 mM concentration were added to the protein 15–30 min before the grid preparation and the samples were incubated on ice. Protein sample (2.7 μl) was applied to a freshly glow-discharged Quantifoil 0.6/1 copper grid and blotted for 4–6 s using a blotting force of 25 at 4 °C and 100% humidity in an Vitrobot Mark IV (FEI). Grids were flash-frozen in liquid ethane and stored in liquid nitrogen until data collection. NNT–$NADP^+$ grids were imaged using a 300 kV Titan Krios electron microscope equipped with a Gatan energy-filtered K2 summit camera with a slit width of 20 eV at The Astbury Centre for Structural Molecular Biology of the University of Leeds. NNT–NADPH grids were imaged using a 300 kV Titan Krios electron microscope equipped with a Gatan energy-filtered K2 summit camera with a slit width of 20 eV at the CM01 beamline, ESRF, Grenoble. Images were collected with EPU acquisition software in a K2 super-resolution mode with a nominal magnification of 130,000× and a physical pixel size of 1.065 Å for the NNT–$NADP^+$ dataset and 1.07 Å for the NNT–NADPH dataset. A total dose of 72 e^- $Å^{-2}$ (NNT–$NADP^+$) or 70 e^- $Å^{-2}$ (NNT–NADPH) was fractionated into 40 frames of 250 ms each. Apo-NNT grids were imaged using a 300 kV Titan Krios electron microscope equipped with a Gatan energy filtered K3 camera with a slit width of 20 eV at the Institute of Science and Technology Austria. Physical pixel size was 0.84 Å and the total dose of 90 e^- $Å^{-2}$ was fractionated into 88 frames of 36 ms each.

Image processing. We collected 2,272 movies for the $NADP^+$ dataset, 1,722 movies for the NADPH dataset and 786 movies for the apo-NNT dataset. The processing was carried out in RELION 2.1[33] unless otherwise stated. Movie frames were aligned using MotionCor2[34] and initial contrast transfer function (CTF) parameters were estimated from averaged images using CTFFIND[35]. Autopicking with 2D class averages as references resulted in 516,395 particles for the NADPH dataset, 1,076,677 particles for the $NADP^+$ dataset and 500,001 particles for the apo dataset. Multiple rounds of 2D classification and 3D classification were performed to classify considerably heterogeneous particles in all datasets (Extended Data Figs. 3, 4). CTF parameters and per-particle trajectories in the best two classes from the $NADP^+$ dataset were estimated and corrected (particle polishing) using RELION 3.0[36]. Local resolution was estimated using Resmap 5.0[37].

For the $NADP^+$ dataset we performed one round of 2D classification followed by two rounds of 3D classification with 3× and 2× binned particles, respectively, which resulted in eight classes containing 342,284 particles; from this, it was apparent that there is a considerable heterogeneity in the conformations of dI_2 and dIIIb. To address this, the particles were re-extracted without binning and refined with a dII_2dIII_2 mask to 3.5 Å and then classified into ten classes without searches and without a mask to separate the particles based on the relative position of the dI_2. By combining similar classes and auto-refining them, we separated six different states of NNT which differ from each other with respect to the positions of dI_2 and dIIIb. Two of these classes were resolved to 13 Å, further two to 7 Å and the best two classes to 3.7 and 3.2 Å. From the latter two maps it was obvious that the density for dI_2 was still weaker than for the rest of the particle, indicative of remaining heterogeneity in the positions of dI_2; as such, the final maps for these two classes were produced by combining focus-refined maps of the dII_2dIII_2 and dI_2 parts. This gave the final map for class 1 (double face-down) with 2.9 Å resolution in the dII_2dIII_2 and 3.2 Å resolution in the dI_2 regions, and for class 2 (single face-down) we obtained 3.5 Å resolution for the dII_2dIII and 4.1 Å resolution for the dI_2 regions. Owing to the poor quality of the map for the single face-down class in some regions of dIIb (CL6, 7, 8) we proposed that there remains some conformational heterogeneity present in this class, and we performed another round of classification of these particles with a mask around dIIb to sort out any particles with dIIIb attached or semi-attached to dII. This procedure removed 52% of the particles, and we performed an auto-refinement with a dII_2dIII mask of the remaining 28,498 particles with dIIIb unambiguously detached. This resulted in a 3.7 Å map with the dIIb density much better resolved and clearly different from the density of dIIa (which has dIII attached), and it was subsequently used for model building.

For the NADPH dataset, we performed one round of 2D classification followed by one round of 3D classification on 510,073 3× binned particles with the same parameters as in the $NADP^+$ dataset; this failed to yield any class with visible secondary structural features. We performed extensive classifications of these particles into 4–20 classes with values of the regularization factor T between 4 and 12 and different filtering of the reference volumes, which all failed to give a single well-defined class with secondary structural features. Nevertheless, we selected 405,141 particles from the best 4 classes from a classification with $T = 8$ and $k = 6$ classes (the same as for the $NADP^+$ dataset) for further classification attempts. Another round of extensive classifications was performed on this particle stack, with the best results obtained from a $T = 8$, $k = 20$ run. Even in this run, only around six classes had well-defined features that corresponded to the domains of NNT. These six classes were re-extracted and refined to give structures at 8.3, 9.2, 13, 16, 16, and 16 Å, and revealed a high degree of dI_2 and dIII mobility (Extended Data Fig. 4a). To address this, we tried to refine the 405,141 particles together into one consensus structure at 13 Å, followed by focused refinement of either dI_2 or dII_2; however, neither of these strategies yielded structures with a resolution better than 9 Å, probably because the conformational heterogeneity within the consensus refinement was too large. Furthermore, the molecular masses of dI_2 and dII_2 are only 80 kDa, and dII_2 is obscured by a micelle, which further complicates the alignment of such a heterogeneous dataset. Finally, we performed multi-body refinement in RELION 3.0 starting from the consensus refinement of 405,141 particles and using masks for the two bodies dI_2 and dII_2. This yielded a 9 Å reconstruction of dI_2 and a 10 Å reconstruction of dII_2, but more importantly, the principal component analysis showed a high degree of dI_2 mobility in these particles (Fig. 2b). This is not unexpected because, upon dIII dissociation, dI_2 remains only loosely tethered to the rest of the particle by a flexible dI–dII linker.

The apo-NNT dataset was fully processed in RELION 3.0. We manually selected 643 good images and extracted 3× binned particles. Only one conformation of NNT could be observed using various 3D classification schemes, hence the 283,706 particles corresponding to it were extracted without binning and were auto-refined to 4.5 Å. From this structure it was clear that dI_2 exhibits the same heterogeneity as in the $NADP^+$ dataset. To improve the resolution in the dII–dIII, we focus-refined around this region and classified the particles without searches into six classes. The best class, with 67,908 particles, was auto-refined and polished to reach a resolution of 3.7 Å. Further polishing or subclassification of this class did not improve the resolution further. Attempts at focus-refinement of dI_2 did not improve its resolution compared to the polished full structure of the final selected particles, in which local resolution in dI_2 was around 5 Å. We conclude that dI_2 without bound nucleotide exhibits even more disorder than when NAD^+ is bound, possibly enabling NAD(H) exchange and dI_2 binding and release.

Model building and refinement. The initial model was built into the double face-down $NADP^+$ class density by starting with the bovine dIII crystal structure with substituted ovine sequence and the dI homology model that was generated using Phyre2 server[38]. The dII model and the linkers were built manually in Coot[39]. Manually adjusted models were refined using *PHENIX* software[40] using an adapted method for refining cryo-EM structures, which uses two rounds of a single cycle of group ADP

refinement followed by three cycles of global minimization. This enables optimization of B-factors so that electron radiation-damaged carboxylate side-chains acquire high B-factors and do not lead to main-chain distortions[41]. The final model of NNT is of very high quality in terms of geometry and fit to density (Supplementary Table 1).

Densities for several lipid molecules were observed in each of the half-closed cavities formed by helices TM1, TM2 and TM6 (Extended Data Figs. 5g, 6g, h). They were modelled in the structure as phosphatidylcholines on the basis of the appearance of their density and the fact that only phosphatidylcholine could reactivate lipid-depleted insect NNT[42].

A density corresponding to the adenylate part of NAD^+ was observed in the NAD(H) binding site of the dI (Extended Data Fig. 5j, k). We propose that this density is NAD^+ that remained bound to the enzyme during purification or, more likely, was introduced into the sample as a contaminant from the $NADP^+$ solution. Our $NADP^+$ was only 98% pure and, at 2% NAD^+ contamination, the NAD^+ concentration would be 100 μM, which is in the range of the K_d for the enzyme[23,28]. The latter proposal is supported by the fact that, in our structure, the conserved R139 is in the same extended conformation as in the *Escherichia coli* dI_2 with bound NAD^+, and differs considerably from the apo or NADH-bound forms[13]. Nevertheless, our structure is a bona fide oxidized ground-state conformation of NNT, and earlier biochemical work suggests that nucleotide exchange in the dI subunit can occur during any stage of the catalytic cycle and does not influence the global conformation of the enzyme[15,16,43,44]. Models for the single face-down $NADP^+$ class and the apo NNT were based on the double face-down NNT as the starting model. For apo NNT, owing to the lack of reliable amino acid side-chain information in the cryo-EM density of the dI domain, dI was modelled as a polyalanine model based on the dI from the PDB structure 6QTI, and was fit into the density as a rigid body.

Structure analysis and preparation of figures. Evolutionary conservation scores were projected onto the transhydrogenase structure using ConSurf[45] (Extended Data Fig. 1b). Buried water molecules were modelled using the original Dowser software[46] (Fig. 3, Extended Data Fig. 7). The proton translocation pore was predicted and analysed using a MOLEonline server[47]. Interdomain contacts and binding energy of nucleotides were analysed using the PISA server[48,49]. Models were evaluated using MolProbity and EMRinger[50,51]. Clustal Omega was used for sequence alignment[52,53]. Models and density maps were visualized for analysis and figure preparation purposes in PyMOL 2.2.3 and UCSF Chimera[54].

Activity measurements and trypsinolysis. Reverse transhydrogenation activity was measured spectrophotometrically at 30 °C by following the reduction of $APAD^+$ (3-acetylpyridine adenine dinucleotide; NAD^+ analogue; extinction coefficient $\varepsilon = 5.1\ mM^{-1}\ cm^{-1}$) at 375 nm using a Shimadzu UV-2600 UV-VIS spectrophotometer. Background absorption at 455 nm was subtracted from absorption at 375 nm. The reaction buffer was similar to the minimal EDTA-containing buffer used in a previous publication, with a change in detergent and buffering agent to maximise activity (20 mM Tris-HCl, pH 6.8, 50 mM NaCl, 0.5 mM EDTA, 0.1% CHAPS, 0.25 mg ml^{-1} lipids, 100 μM NADPH and 100 μM $APAD^+$)[25]. For lipids we used soybean asolectin or a 4:1 mixture of 1,2-dioleoyl-*sn*-glycero-3-phosphocholine:cardiolipin (DOPC:CL) with similar results. The reaction was started with the addition of NNT. The activity depended on the type of detergent used during the final size-exclusion chromatography step. Preparations in FOM gave slightly higher activity (around 20 U mg^{-1}) than those in LMNG (around 15 U mg^{-1}). These values compare favourably to previous measurements[25,55].

Trypsinolysis was performed as described previously with a few changes[15]. NNT at 0.05 mg ml^{-1} in GF buffer with 1 mM HEPES pH 7.4 was incubated with 0.4 mM nucleotides, trypsin (at different mass ratios) and 60 mM BAT buffer (1:1:1 Bis-Tris, acetate, tricine) at pH 5–8. Because the optimum pH of trypsin is around 8, mass ratios between 1:400 and 1:40 and incubation times between 30 and 60 min were used at different pH values to achieve comparable rates of proteolysis.

Reconstitution of proteoliposomes. NNT was reconstituted into proteoliposomes using a detergent dilution procedure as described before[25]. In brief, NNT purified in FOM or in LMNG was mixed with a 500-fold excess of DOPC solubilized in 1% CHAPS. After a 10-min incubation on ice, the solution was diluted 100-fold and incubated on ice for 3–5 h before measuring the activities. The reaction was started by substrate addition (NADPH and $APAD^+$ at 100 μM). Carbonyl cyanide 3-chlorophenylhydrazone (CCCP; 10 μM) was added after 1 min to decouple the proton gradient across proteoliposomes to assess the dependence of the transhydrogenation reaction on the proton motive force. After another 1 min, CHAPS (0.05%) was added to solubilize proteoliposomes and give a total decoupled reverse transhydrogenation activity of both inward- and outward-facing transhydrogenases.

Reporting Summary. Further information on research design is available in the Nature Research Reporting Summary linked to this article.

Data availability

Structures of 'double face-down' and 'single face-down' $NADP^+$ states and apo-NNT have been deposited in the Protein Data Bank with accession numbers 6QTI, 6QUE and 6S59, respectively. The corresponding cryo-EM density maps in have been deposited in the Electron Microscopy Data Bank with accession numbers EMD-4635, EMD-4637 and EMD-10099.

31. Smith, A. L. Preparation, properties, and conditions for assay of mitochondria: Slaughterhouse material, small-scale. *Methods Enzymol.* **10**, 81–86 (1967).
32. Letts, J. A., Degliesposti, G., Fiedorczuk, K., Skehel, M. & Sazanov, L. A. Purification of ovine respiratory complex I results in a highly active and stable preparation. *J. Biol. Chem.* **291**, 24657–24675 (2016).
33. Scheres, S. H. W. RELION: implementation of a Bayesian approach to cryo-EM structure determination. *J. Struct. Biol.* **180**, 519–530 (2012).
34. Zheng, S. Q. et al. MotionCor2: anisotropic correction of beam-induced motion for improved cryo-electron microscopy. *Nat. Methods* **14**, 331–332 (2017).
35. Rohou, A. & Grigorieff, N. CTFFIND4: Fast and accurate defocus estimation from electron micrographs. *J. Struct. Biol.* **192**, 216–221 (2015).
36. Zivanov, J. et al. New tools for automated high-resolution cryo-EM structure determination in RELION-3. *eLife* **7**, e42166 (2018).
37. Kucukelbir, A., Sigworth, F. J. & Tagare, H. D. Quantifying the local resolution of cryo-EM density maps. *Nat. Methods* **11**, 63–65 (2014).
38. Kelley, L. A., Mezulis, S., Yates, C. M., Wass, M. N. & Sternberg, M. J. E. The Phyre2 web portal for protein modeling, prediction and analysis. *Nat. Protoc.* **10**, 845–858 (2015).
39. Emsley, P., Lohkamp, B., Scott, W. G. & Cowtan, K. Features and development of Coot. *Acta Crystallogr. D* **66**, 486–501 (2010).
40. Adams, P. D. et al. *PHENIX*: a comprehensive Python-based system for macromolecular structure solution. *Acta Crystallogr. D* **66**, 213–221 (2010).
41. Letts, J. A., Fiedorczuk, K., Degliesposti, G., Skehel, M. & Sazanov L. A. Structures of respiratory supercomplex $I+III_2$ reveal functional and conformational crosstalk. *Mol. Cell* (in the press).
42. Vandock, K. P., Emerson, D. J., McLendon, K. E. & Rassman, A. A. Phospholipid dependence of the reversible, energy-linked, mitochondrial transhydrogenase in *Manduca sexta*. *J. Membr. Biol.* **242**, 89–94 (2011).
43. Hu, X., Zhang, J. W., Persson, A. & Rydström, J. Characterization of the interaction of NADH with proton pumping *E. coli* transhydrogenase reconstituted in the absence and in the presence of bacteriorhodopsin. *Biochim. Biophys. Acta Bioenerg.* **1229**, 64–72 (1995).
44. Tong, R. C. W., Glavas, N. A. & Bragg, P. D. Topological analysis of the pyridine nucleotide transhydrogenase of *Escherichia coli* using proteolytic enzymes. *Biochim. Biophys. Acta* **1080**, 19–28 (1991).
45. Landau, M. et al. ConSurf 2005: the projection of evolutionary conservation scores of residues on protein structures. *Nucleic Acids Res.* **33**, W299–W302 (2005).
46. Zhang, L. & Hermans, J. Hydrophilicity of cavities in proteins. *Proteins* **24**, 433-438 (1996).
47. Pravda, L. et al. MOLEonline: a web-based tool for analyzing channels, tunnels and pores (2018 update). *Nucleic Acids Res.* **46**, W368–W373 (2018).
48. Krissinel, E. & Henrick, K. Inference of macromolecular assemblies from crystalline state. *J. Mol. Biol.* **372**, 774–797 (2007).
49. Krissinel, E. Crystal contacts as nature's docking solutions. *J. Comput. Chem.* **31**, 133–143 (2010).
50. Barad, B. A. et al. EMRinger: side chain-directed model and map validation for 3D cryo-electron microscopy. *Nat. Methods* **12**, 943–946 (2015).
51. Chen, V. B. et al. MolProbity: all-atom structure validation for macromolecular crystallography. *Acta Crystallogr. D* **66**, 12–21 (2010).
52. Goujon, M. et al. A new bioinformatics analysis tools framework at EMBL-EBI. *Nucleic Acids Res.* **38**, W695–W699 (2010).
53. Larkin, M. A. et al. Clustal W and Clustal X version 2.0. *Bioinformatics* **23**, 2947–2948 (2007).
54. Pettersen, E. F. et al. UCSF Chimera—a visualization system for exploratory research and analysis. *J. Comput. Chem.* **25**, 1605–1612 (2004).
55. Wu, L. N. Y., Alberta, J. A. & Fisher, R. R. Purification and reconstitution of bovine heart mitochondrial transhydrogenase. *Methods Enzymol.* **126**, 353–360 (1986).

Acknowledgements We thank R. Thompson, G. Effantin and V.-V. Hodirnau for their assistance with collecting $NADP^+$, NADPH and apo datasets, respectively. Data processing was performed at the IST high-performance computing cluster. This project has received funding from the European Union's Horizon 2020 research and innovation programme under the Marie Skłodowska-Curie Grant Agreement no. 665385.

Author contributions D.K. purified transhydrogenase, prepared cryo-EM grids, acquired and processed EM data, built and analysed the atomic models and wrote the initial draft of the manuscript. L.A.S. designed and supervised the project, acquired funding, analysed data and revised the manuscript.

Competing interests The authors declare no competing interests.

Additional information

Supplementary information is available for this paper at https://doi.org/10.1038/s41586-019-1519-2.

Correspondence and requests for materials should be addressed to L.A.S.

Peer review information *Nature* thanks Amandine Marechal and the other, anonymous, reviewer(s) for their contribution to the peer review of this work.

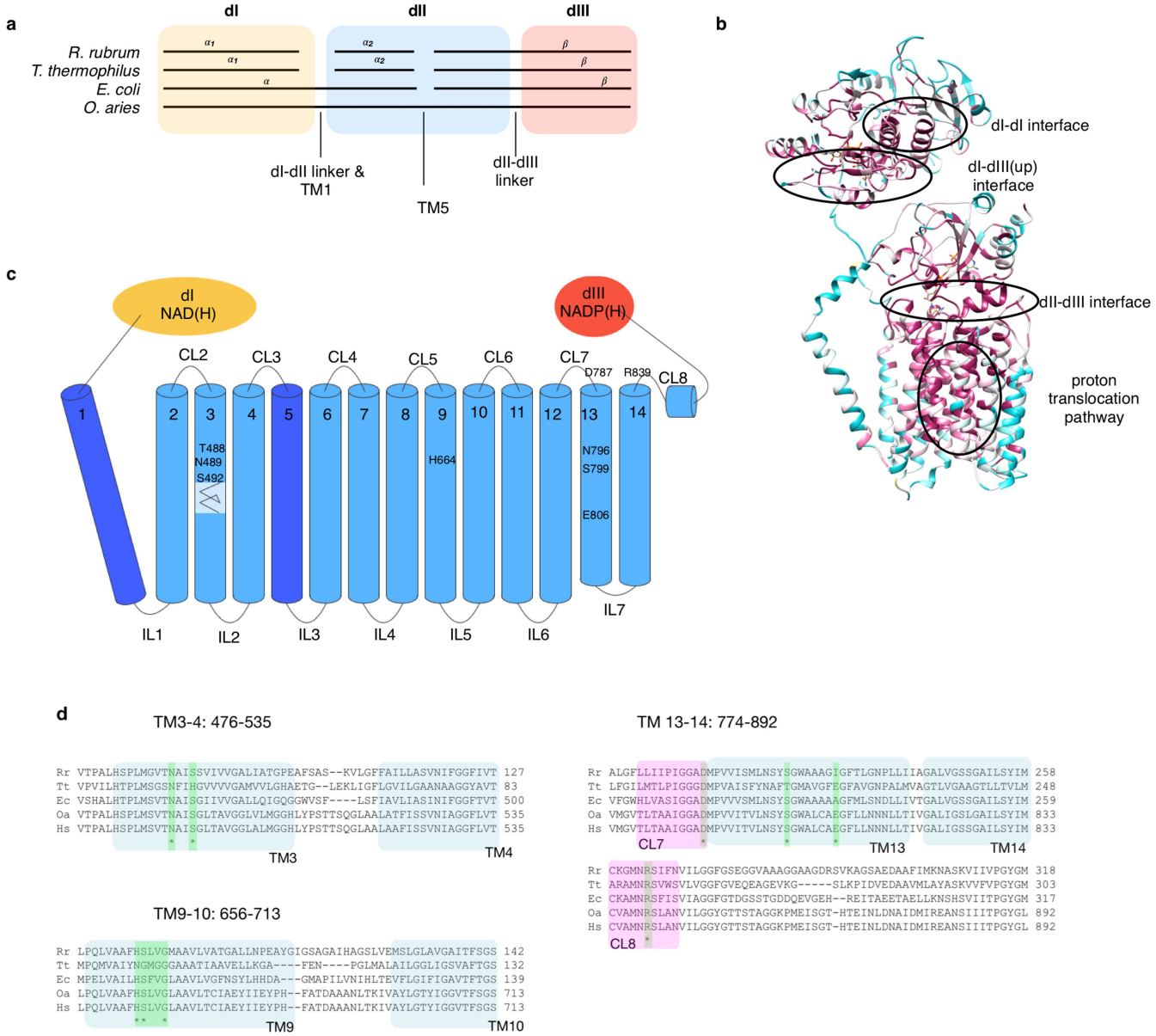

Extended Data Fig. 1 | Comparison of model transhydrogenases from different species. a, The domain split and organization of transhydrogenase in the four model species: *T. thermophilus*, *Rhodospirillum rubrum*, *E. coli* and *Ovis aries*. The dII–dIII linker is conserved in all transhydrogenases, whereas the dI–dII linker and TM1 are limited to NNTs with an α-β polypeptide split (for example, *E. coli*) and single-polypeptide NNTs (metazoans, including mammals). TM5 is present only in metazoans. **b**, Residue conservation scores (calculated in Consurf, coloured cyan to magenta from low to high conservation) mapped on the structure of a single monomer of transhydrogenase. The most highly conserved regions are the proton translocation pathway, the nucleotide binding sites and the dI–dIII, dII–dIII and dI–dI interfaces. **c**, The architecture of mammalian dII. Supernumerary helices TM1 and TM5 are coloured in a darker shade of blue. Residues of the proton transfer pathway are labelled in the helices. The 3_{10}-helix stretch within TM3 is depicted as a triangular helix. **d**, Alignment of conserved residues on TM3, TM9, TM13, TM14 and CL7 and CL8 important for proton translocation and reaction coupling in *T. thermophilus* (Tt), *R. rubrum* (Rr), *E. coli* (Ec), *O. aries* (Oa) and *Homo sapiens* (Hs). *T. thermophilus* and a few other species with an NGXGG motif on TM9 have the protonatable histidine on TM3 (α_2H42 in *T. thermophilus*), whereas most other species that share an HSXXG motif on TM9 have the protonatable histidine on TM9 (βH91 in *E. coli* and H664 in *O. aries*).

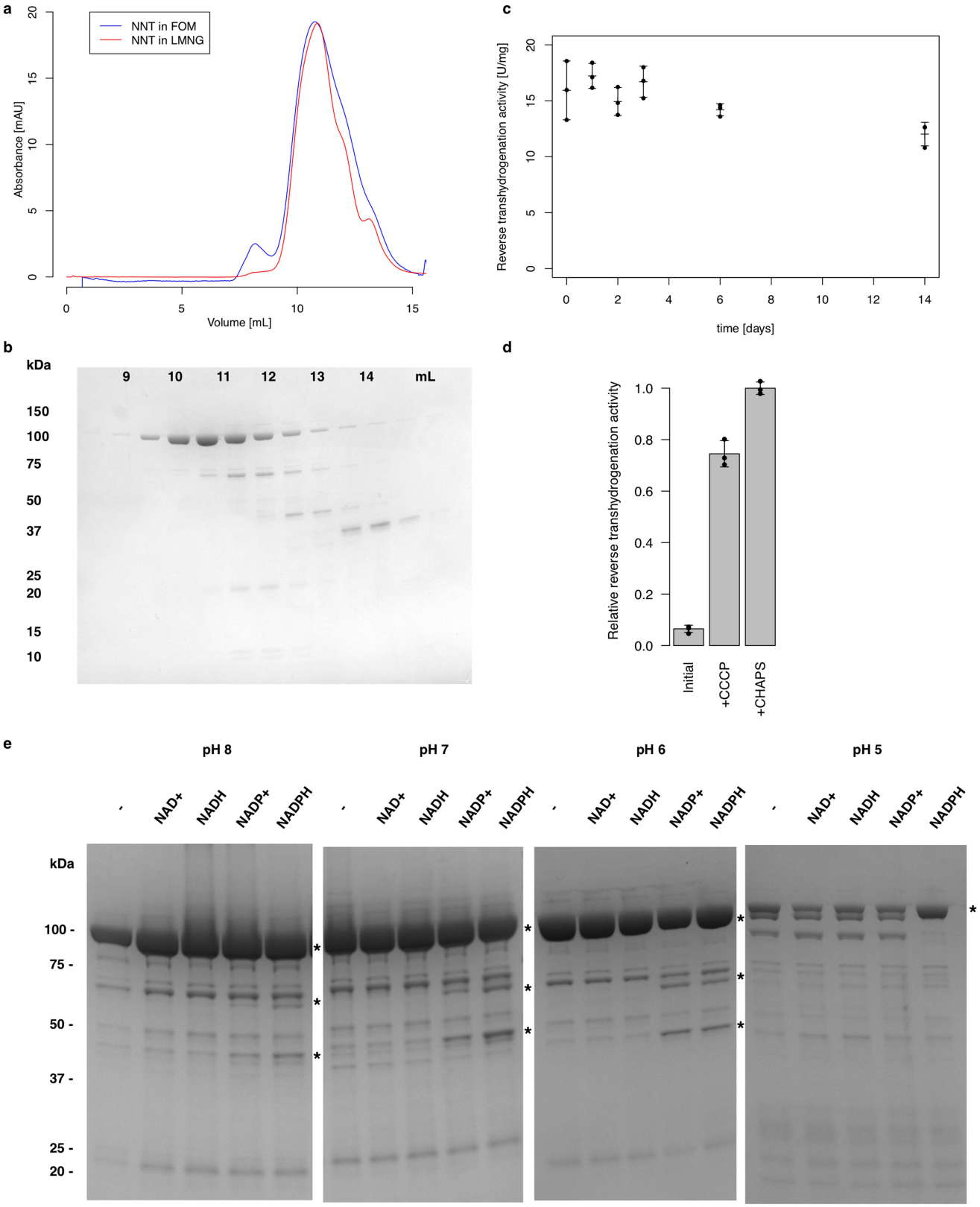

Extended Data Fig. 2 | See next page for caption.

Extended Data Fig. 2 | Purification and biochemical characterization of ovine transhydrogenase. a, Ovine NNT was purified chromatographically. The last step of purification—size-exclusion chromatography—is shown in two different detergents, FOM and LMNG. **b**, SDS–PAGE shows the presence of an approximately 110 kDa polypeptide of NNT. The highest purity fractions (which eluted at around 10.5 ml) were pooled and concentrated for cryo-EM sample preparation. **c**, NNT is highly active and stable when purified in LMNG as shown by undiminished activity over several days when stored at 4 °C. Error bars represent standard deviations based on $n = 3$ independent measurements. **d**, Reconstitution of purified NNT into DOPC liposomes shows that the reverse transhydrogenation reaction is tightly coupled to proton transfer, as it is stimulated around tenfold by the proton-gradient uncoupler CCCP and by solubilisation in CHAPS detergent. Error bars represent standard deviations based on $n = 3$ independent measurements. **e**, Trypsinolysis of NNT at different pH values in the presence of substrates. The full NNT (110 kDa) and previously identified[15] fragments at 66 and 43 kDa are labelled with asterisks. As the pH decreases from 8 to 6, NADPH-induced proteolysis diminishes relative to that induced by $NADP^+$. At pH 5 trypsin produces different fragments, but stabilization of the intact NNT by NADPH is evident. Trypsinolysis was performed independently three times with similar results. The purification of NNT was repeated independently ten times with similar results as shown in **a**, **b**. For gel source data, see Supplementary Fig. 1.

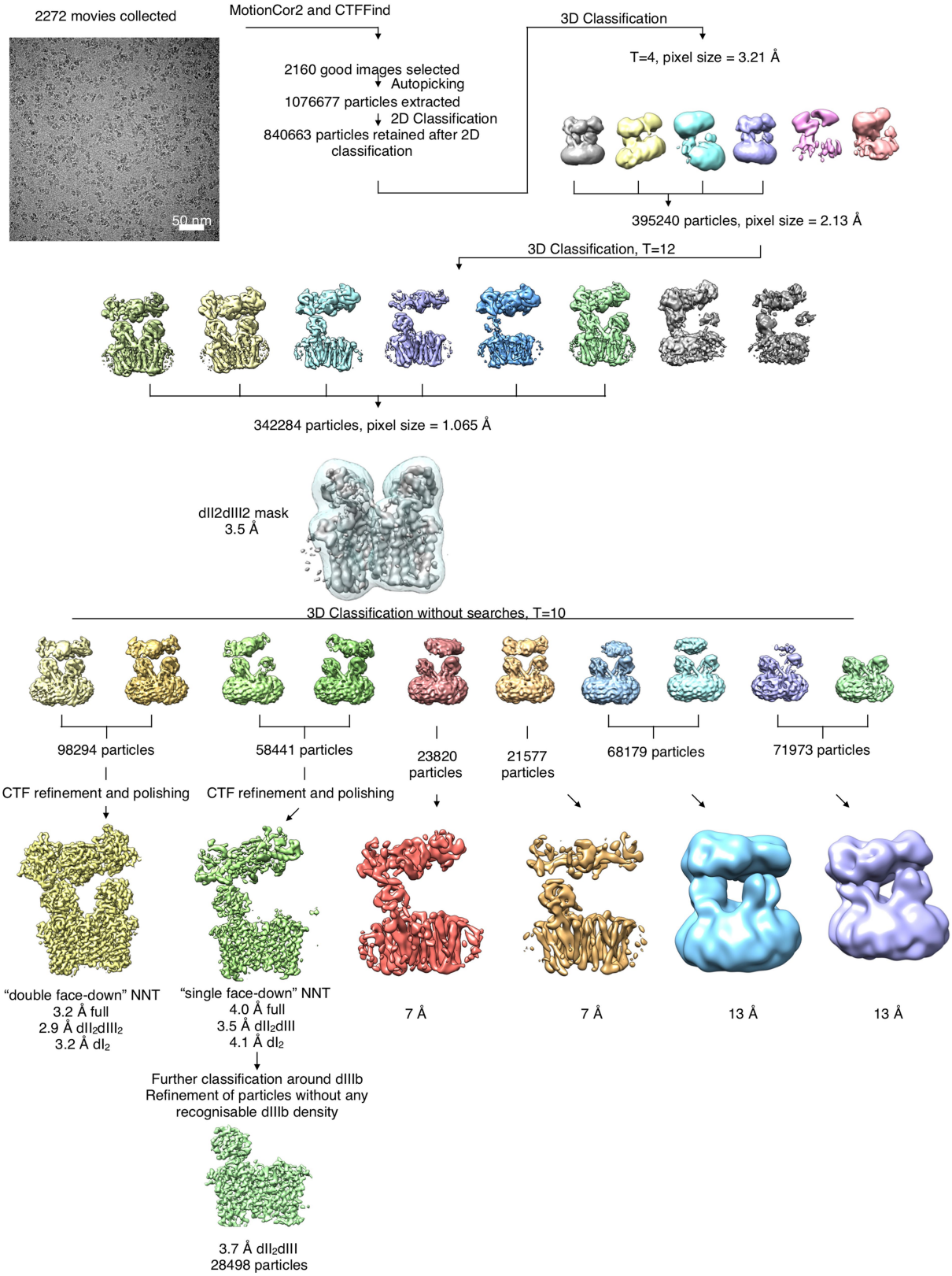

Extended Data Fig. 3 | Processing of the NNT–NADP$^+$ dataset. Thorough classification of particles resulted in six distinct classes with different domain orientations and resolutions. The best-resolution class (double face-down NNT) is almost symmetric with both dIIIs bound in the face-down position, whereas the other five have only one dIII bound in the face-down position, with the other dIII detached and the dI_2 tilted at different angles. Simultaneous tilting of dI_2 and dissociation of dIIIb is probably necessary to permit full dIIIb rotation during the catalytic cycle. Monomers with dIII detached from dII also show little or no density for the dI–dII linker, which suggests that it detaches from dIII to enable dI_2 to open.

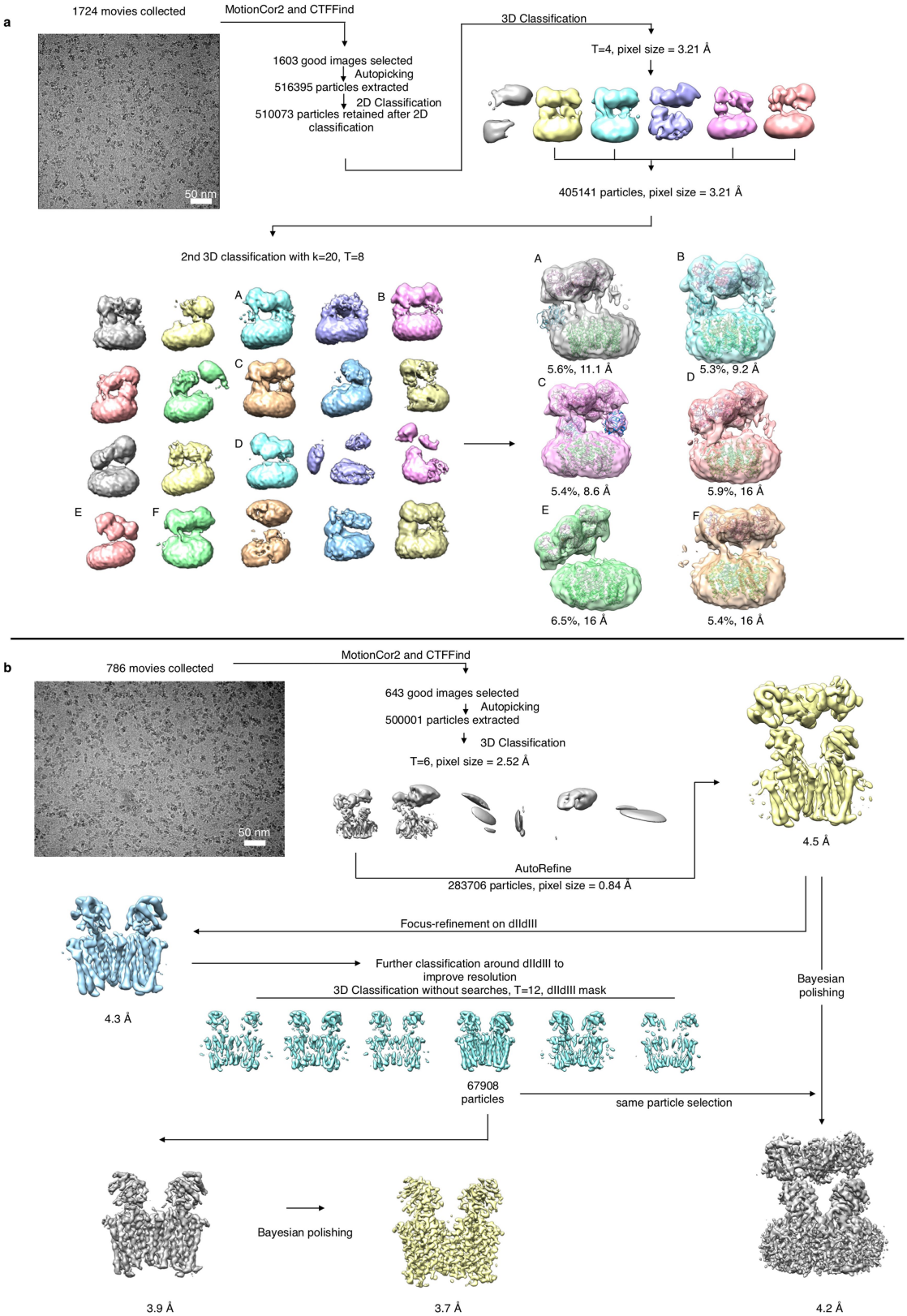

Extended Data Fig. 4 | Processing of NNT–NADPH and Apo-NNT datasets. a, NNT bound to NADPH exhibited a large degree of conformational flexibility, which prevented a high-resolution (beyond 8 Å) refinement of any class of particles. Classification into 20 classes revealed that only a small proportion (around 5%) of particles have one dIII bound to dII in the face-down orientation (class C). About another 10% have partially detached dIII (classes A and B). The majority, however, have both dIIIs dissociated from the other domains, leading to a large degree of freedom of movement of dI_2 and of both dIIIs independent of each other (see classes D, E and F). **b**, Apo-NNT exhibited a single conformational class, similar to the double face-down NNT class in the presence of $NADP^+$.

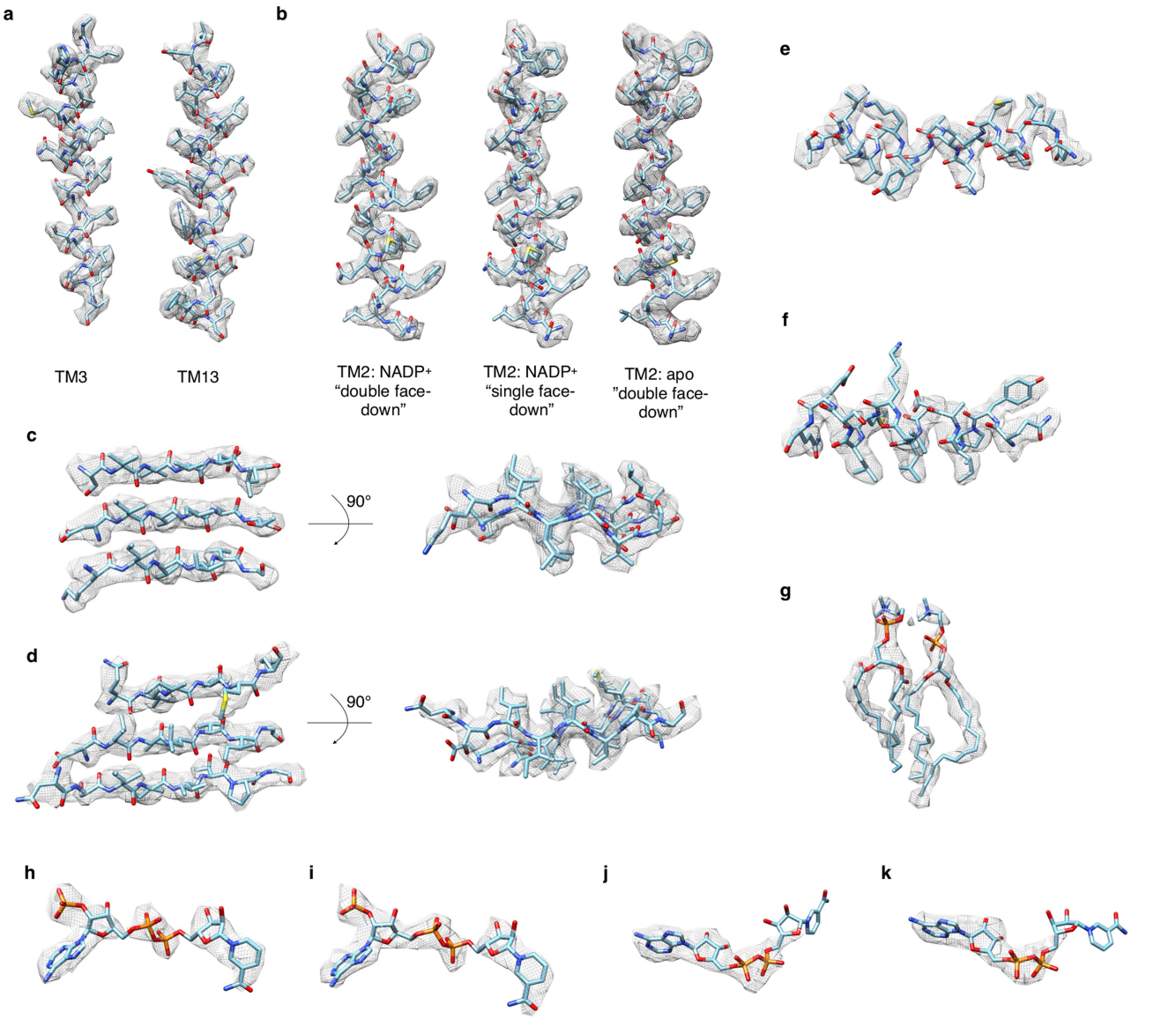

Extended Data Fig. 5 | Examples of cryo-EM density of protein and ligand. All examples are from the double face-down class in the presence of $NADP^+$, unless otherwise stated. **a**, Density of the transmembrane helices that line the proton channel (TM3 and TM13). **b**, Comparison of density of the TM2 between the double face-down and the single face-down (dIII-detached monomer) $NADP^+$ classes, as well as the apo class, which remains in the same conformation upon dII opening while TM9 changes (Extended Data Fig. 6c). **c**, Beta-sheet density of dI. **d**, Beta-sheet density of dIII. **e**, α-helical segment density of dI. **f**, α-helical segment density of dIII. **g**, Two phosphatidyl cholines bound in the cavity enclosed by TM1, TM2 and TM6. **h**, Density of dIIIa–$NADP^+$. **i**, Density of dIIIb–$NADP^+$. **j**, Partial NAD^+ density in dIa. **k**, Partial NAD^+ density in dIb. The density for lipids and putative NAD^+ is discussed in Methods.

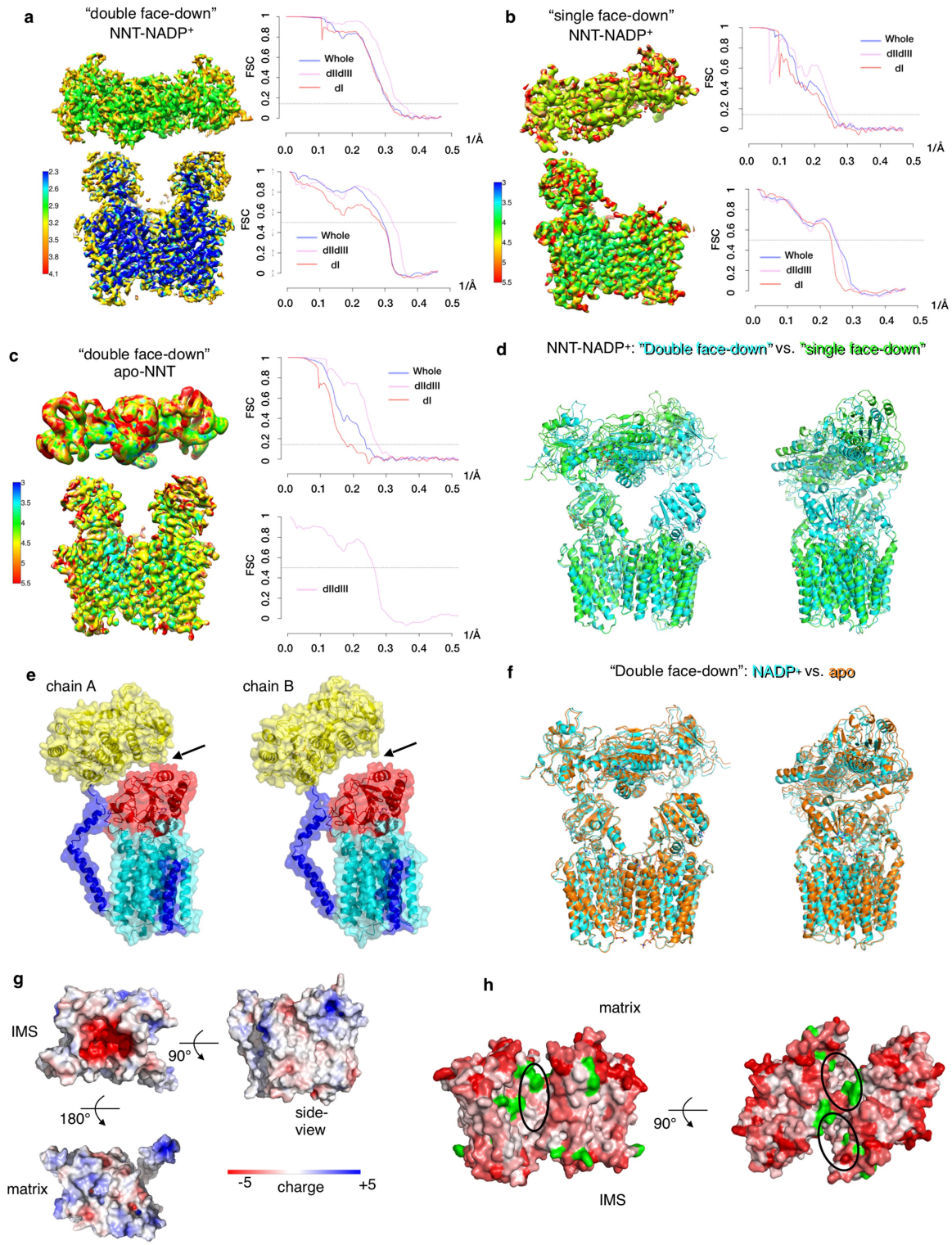

Extended Data Fig. 6 | Comparison of double face-down and single face-down NNT–NADP$^+$ conformations and apo-NNT. a, Local resolution and Fourier shell correlation (FSC) curves for the double face-down NNT–NADP$^+$ structure. **b**, Local resolution and FSC curves for the single face-down NNT–NADP$^+$ structure. **c**, Local resolution and FSC curves for the apo-NNT structure. **d**, Overall comparison of double face-down (cyan) and single face-down (green) classes of NNT. An increased dI tilt, dIIIb detachment and dIIb conformation change are visible. **e**, Comparison of the two monomers in the closed NADP$^+$ class, as viewed from the dimerization interface reveals a tilt of dI_2 and asymmetry in dI-dIIIa/b contacts. **f**, Overall comparison of double face-down NNT–NADP$^+$ (cyan) and apo-NNT. dII and dIII are in the same conformation and dI_2 is slightly more tilted in apo-NNT. **g**, Electrostatic surface potential of the proton entry cavities on the matrix (bottom) and IMS sides (top) as well as that of the membrane-facing side (right). **h**, Hydrophobicity of residues on the surface of dII_2 (coloured white to red from hydrophobic to hydrophilic). Surface-exposed tyrosine and tryptophan residues, which often delineate the surface of the lipid membrane, are highlighted in green and the lipid-binding pocket is circled.

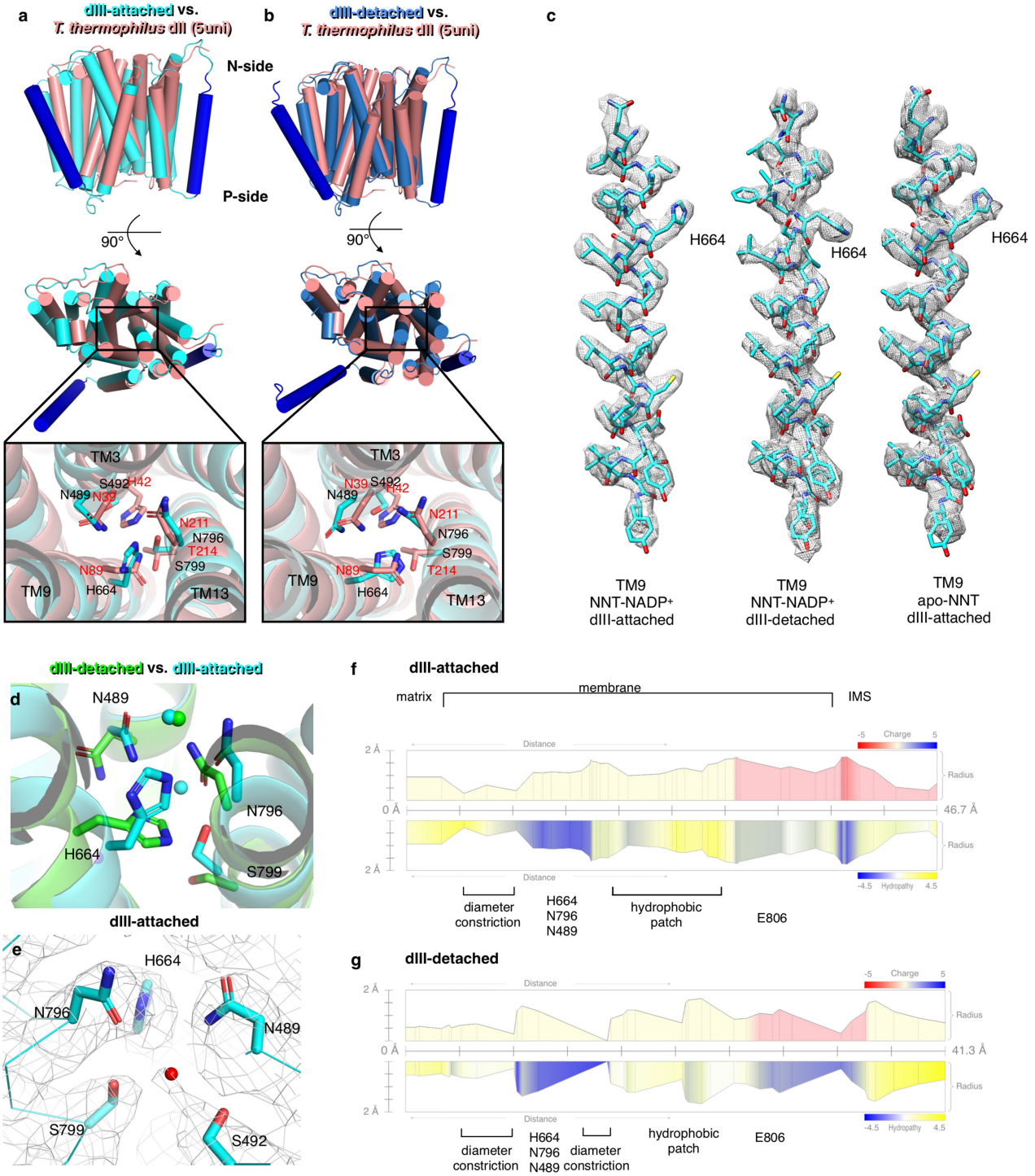

Extended Data Fig. 7 | Changes in the proton translocation channel upon dIII detachment and comparison between ovine and *T. thermophilus* dII. a, Comparison of *T. thermophilus* dII (salmon, PDB: 5UNI) and double face-down (dIII attached) ovine dII (cyan, supernumerary TM1 and TM5 in blue). Residues in the N side cavity display markedly different conformations. **b**, Comparison of *T. thermophilus* dII (salmon, PDB: 5UNI) and single face-down (dIII-detached monomer) ovine dII (blue). Residues in the N side cavity match more closely as both of these dII structures are detached from dIII. **c**, Comparison of the TM9 density in the double face-down, single face-down (dIII-detached monomer) and apo dII clearly displaying a H664 flip in the dIII-detached dII. **d**, Comparison of Dowser-predicted waters in the dIII-attached (cyan) and dIII-detached (green) dII. The dIII-attached structure has two water molecules—one below and one above the N side proton gate—whereas the dIII-detached structure only has one water molecule above the gate, which is consistent with the proposal that the channel is open to the P side when dIII is attached. **e**, Density for a water molecule coordinated between H664 and S492, consistent with Dowser-predicted water, is beginning to show in our cryo-EM density. **f**, Proton pathway profile (calculated in Mole 2.5) in dIII-attached dII reveals a diameter constriction between the N side and H664, a hydrophobic stretch between H664 and E806 and a negatively charged P side proton-entry site. **g**, Proton pathway profile in the dIII-detached dII. Additional constriction appearing between H664 and the P side upon dIII detachment is indicated.

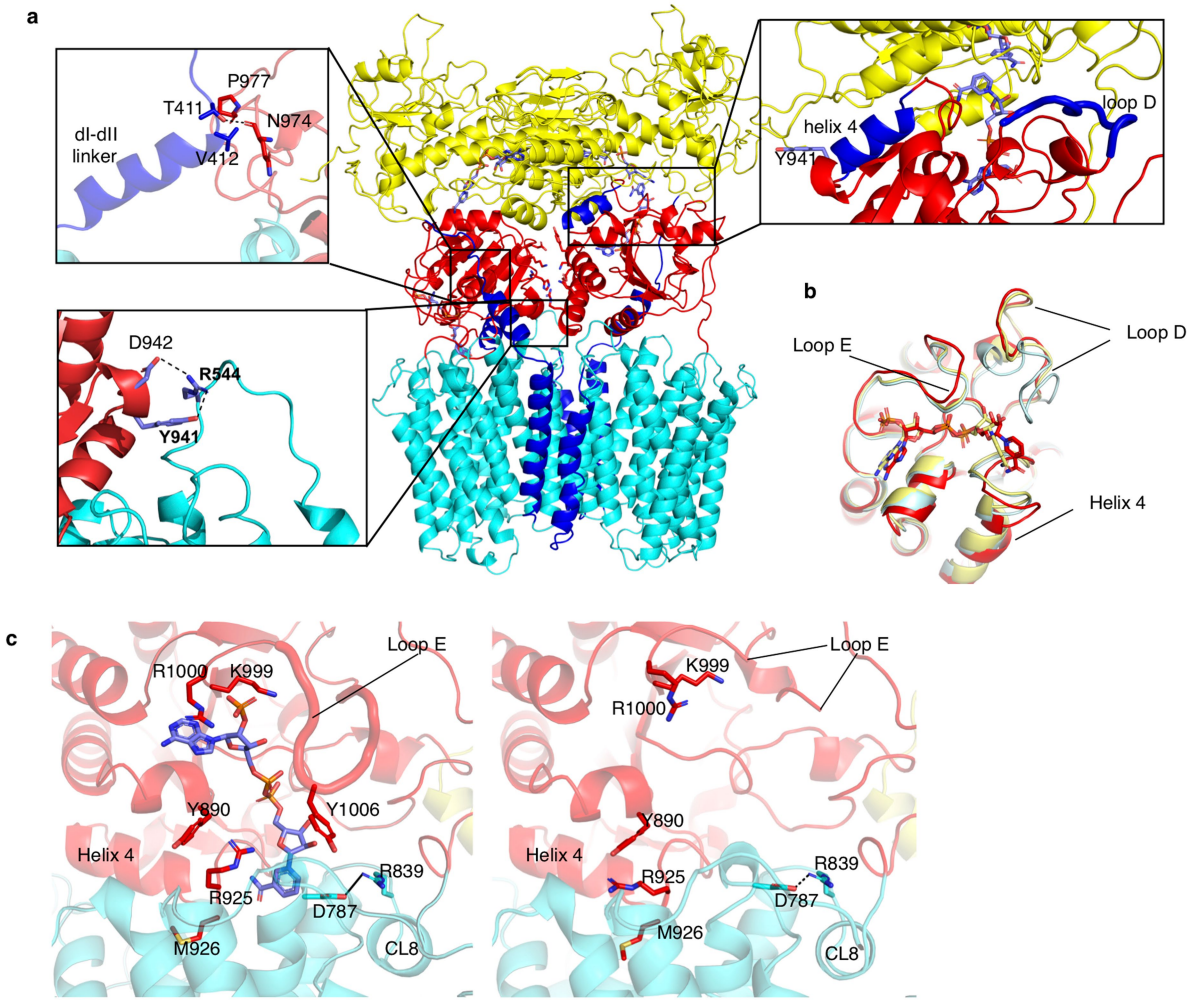

Extended Data Fig. 8 | Different conformations of dIII. a, A homology model of the asymmetric ovine NNT based on the *T. thermophilus* dI_2dIII heterotrimer structure (PDB: 4J16). Note the putative interacting residues at the dIIIup–dIIIdown interface. The dI–dII linker contacts the loop D of dIII in the face-down conformation. D942 and Y941 from dIII form hydrogen bonds with R544 on the CL2 loop, which stabilizes the dII–dIII interface. Helix 4 and loop D also contribute towards formation of the dI–dIII interface, but Y941 is too far away to interact with dI. **b**, Comparison of ovine dIII (red) with dIII isolated from *R. rubrum* (PDB: 1PNO; chain A in blue and chain B in green). Helix 4, loop D and loop E are all more open around the nucleotide in the ovine structure, but the nucleotide is occluded by the interactions from the dII residues (not shown) in the ovine face-down structure. **c**, Comparison of the NADP(H) binding site in double face-down NNT (left) and apo-NNT (right). Loop E, K999 and R1000 are disordered in apo-NNT and R925 flips into an outward-facing orientation, opening the site to the solvent.

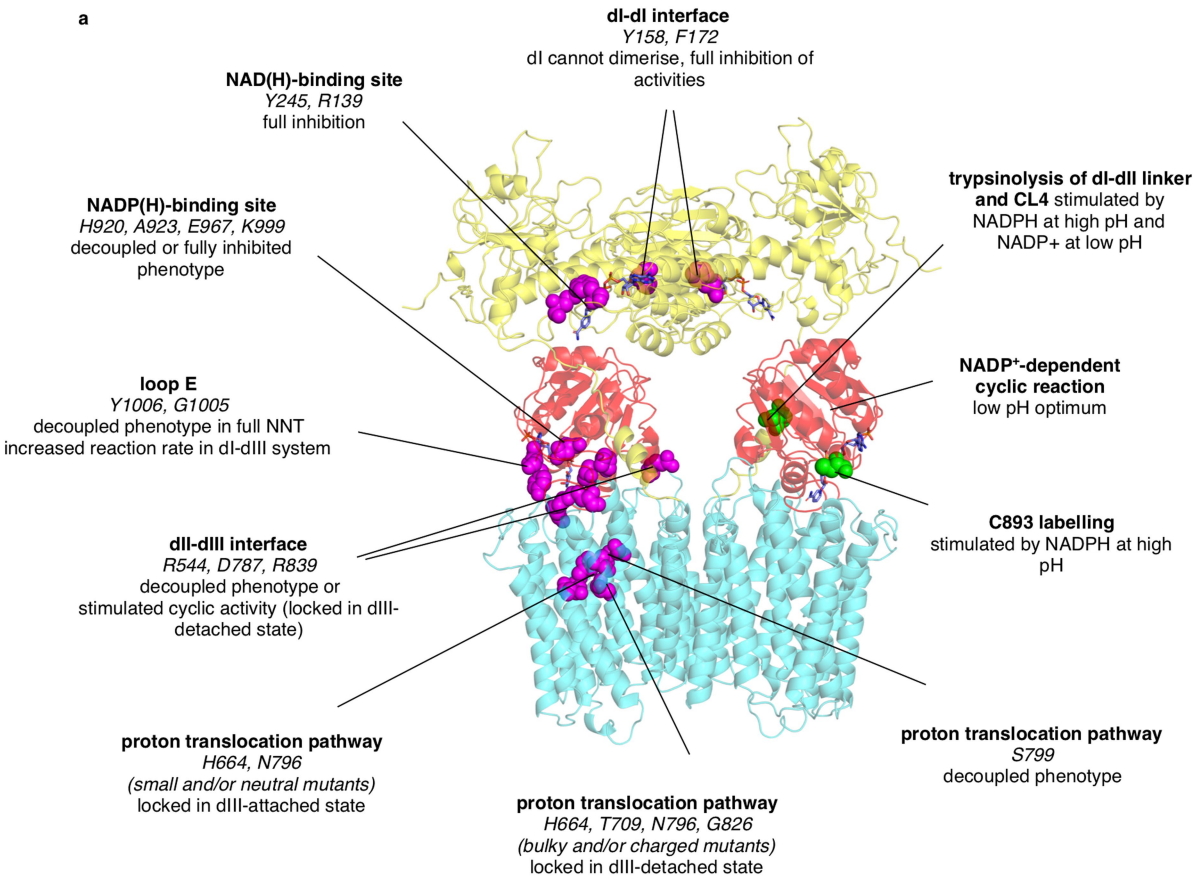

Extended Data Fig. 9 | Validation of the mechanism and the reverse transhydrogenation mechanism. a, Summary of the biochemical evidence and mutagenesis data supporting the proposed mechanism. A full description of mutants in *E. coli*, *R. rubrum* and human patients are provided in Supplementary Tables 1–3. **b**, Our proposal for the reverse reaction. The reverse transhydrogenation reaction consumes NADPH and NAD^+ and results in proton pumping, supporting the proton motive force. The driving forces for this reaction are the nucleotide ratios and low proton motive force, which promotes protonation of H664 from the matrix side.

Extended Data Table 1 | Cryo-EM data collection, refinement and validation statistics

	NNT-NADP+ "double face-down" (EMD-4635) (PDB 6QTI)	NNT-NADP+ "single face-down" (EMD-4637) (PDB 6QUE)	Apo-NNT "double face-down" (EMDB-10099) (PDB 6S59)
Data collection and processing			
Magnification	130000x	130000x	130000x
Voltage (kV)	300	300	300
Electron exposure (e–/Å^2)	72	72	90
Defocus range (μm)	~ -1 to -2.5	~ -1 to -2.5	~ -1 to -2.5
Pixel size (Å)	1.065	1.065	0.84
Symmetry imposed	C1	C1	C1
Initial particle images (no.)	1076677	1076677	500001
Final particle images (no.)	98294	58441	67908
Map resolution (Å)	dI_2 – 3.2 Å, dII_2dIII_2 – 2.9 Å	dI_2 – 4.2 Å, dII_2dIII – 3.7 Å	dI_2 – 4.5 Å, dII_2dIII_2 – 3.7 Å
FSC threshold	0.143	0.143	0.143
Refinement			
Initial model used (PDB code)	dI and dII built de novo, dIII based on 1D4O	6QTI	6QTI
Model resolution (Å)	dI_2 – 3.4 Å, dII_2dIII_2 – 3.1 Å	dI_2 – 4.3 Å, dII_2dIII – 4.0 Å	dII_2dIII_2 – 3.8 Å
FSC threshold	0.5	0.5	0.5
Map sharpening *B* factor (Å^2)	dII_2dIII_2 -36.2 dI_2 -50.2	dII_2dIII -55 dI_2 -77.0	dII_2dIII_2 -67.3 dI_2 -197.5
Model composition			
Non-hydrogen atoms	15996	13791	13397
Protein residues	2076	1865	2066
Ligands	14	3	8
B factors (Å^2)			
Protein	74.0	128.0	115.8
Ligand	114.8	172.8	143.5
R.m.s. deviations			
Bond lengths (Å)	0.0071	0.008	0.0085
Bond angles (°)	1.29	1.30	1.36
Validation			
MolProbity score	1.56	1.66	1.59
EMRinger score	3.58	1.73	2.53
Clashscore	3.37	4.26	3.50
Poor rotamers (%)	0	0.21	0.44
Ramachandran plot			
Favored (%)	93.44	92.85	92.95
Allowed (%)	6.56	7.05	7.05
Disallowed (%)	0	0.1	0

nature research

Corresponding author(s): Leonid Sazanov

Last updated by author(s): Jul 18, 2019

Reporting Summary

Nature Research wishes to improve the reproducibility of the work that we publish. This form provides structure for consistency and transparency in reporting. For further information on Nature Research policies, see Authors & Referees and the Editorial Policy Checklist.

Statistics

For all statistical analyses, confirm that the following items are present in the figure legend, table legend, main text, or Methods section.

n/a	Confirmed	
☐	☒	The exact sample size (*n*) for each experimental group/condition, given as a discrete number and unit of measurement
☐	☒	A statement on whether measurements were taken from distinct samples or whether the same sample was measured repeatedly
☒	☐	The statistical test(s) used AND whether they are one- or two-sided *Only common tests should be described solely by name; describe more complex techniques in the Methods section.*
☒	☐	A description of all covariates tested
☒	☐	A description of any assumptions or corrections, such as tests of normality and adjustment for multiple comparisons
☐	☒	A full description of the statistical parameters including central tendency (e.g. means) or other basic estimates (e.g. regression coefficient) AND variation (e.g. standard deviation) or associated estimates of uncertainty (e.g. confidence intervals)
☒	☐	For null hypothesis testing, the test statistic (e.g. *F*, *t*, *r*) with confidence intervals, effect sizes, degrees of freedom and *P* value noted *Give P values as exact values whenever suitable.*
☒	☐	For Bayesian analysis, information on the choice of priors and Markov chain Monte Carlo settings
☒	☐	For hierarchical and complex designs, identification of the appropriate level for tests and full reporting of outcomes
☒	☐	Estimates of effect sizes (e.g. Cohen's *d*, Pearson's *r*), indicating how they were calculated

Our web collection on statistics for biologists contains articles on many of the points above.

Software and code

Policy information about availability of computer code

Data collection	FEI EPU 1.10
Data analysis	MotionCor2, CTFFIND4, RELION 2.1, RELION 3.0, Chimera, Pymol 2.2.3, Coot 0.8.9, Phenix 1.13, MolProbity, Dowser, MOLEonline 2.5 (webserver), EMRinger (webserver), Clustal Omega (webserver), ConSurf (webserver), PISA (webserver), Phyre2 (webserver), Resmap 5.0

For manuscripts utilizing custom algorithms or software that are central to the research but not yet described in published literature, software must be made available to editors/reviewers. We strongly encourage code deposition in a community repository (e.g. GitHub). See the Nature Research guidelines for submitting code & software for further information.

Data

Policy information about availability of data

All manuscripts must include a data availability statement. This statement should provide the following information, where applicable:

- Accession codes, unique identifiers, or web links for publicly available datasets
- A list of figures that have associated raw data
- A description of any restrictions on data availability

Structures of “double face-down” and “single face-down” NADP+ states and apo-NNT were deposited in PDB with PDB access numbers 6QTI, 6QUE and 6S59, respectively, with corresponding cryo-EM density maps in EMDB (EMD-4635, EMD-4637 and EMD-10099).

Field-specific reporting

Please select the one below that is the best fit for your research. If you are not sure, read the appropriate sections before making your selection.

☒ Life sciences ☐ Behavioural & social sciences ☐ Ecological, evolutionary & environmental sciences

For a reference copy of the document with all sections, see nature.com/documents/nr-reporting-summary-flat.pdf

Life sciences study design

All studies must disclose on these points even when the disclosure is negative.

Sample size	Sample size was determined on the basis of a large number of previous studies using similar methods and dealing with similar proteins.
Data exclusions	No data was excluded from initial analysis. A small number (~5%) of cryoEM movies were excluded after initial analysis steps as they would not contribute meaningfully to the final cryoEM map quality due to poor ice quality or excessive movement.
Replication	Purification of NNT, SDS-PAGE and activity measurements were performed 10 times from two different sources of ovine hearts and all attempts of replication were successful.
Randomization	Samples used in cryo-EM data collection and biochemical assays were equivalent (obtained from the same source and purified by the same method), hence no randomization was necessary.
Blinding	Investigators were not blinded to the sample allocations because all the samples and conditions were predetermined and analysed using the same methods.

Reporting for specific materials, systems and methods

We require information from authors about some types of materials, experimental systems and methods used in many studies. Here, indicate whether each material, system or method listed is relevant to your study. If you are not sure if a list item applies to your research, read the appropriate section before selecting a response.

Materials & experimental systems

n/a	Involved in the study
☒	☐ Antibodies
☒	☐ Eukaryotic cell lines
☒	☐ Palaeontology
☐	☒ Animals and other organisms
☒	☐ Human research participants
☒	☐ Clinical data

Methods

n/a	Involved in the study
☒	☐ ChIP-seq
☒	☐ Flow cytometry
☒	☐ MRI-based neuroimaging

Animals and other organisms

Policy information about studies involving animals; ARRIVE guidelines recommended for reporting animal research

Laboratory animals	*For laboratory animals, report species, strain, sex and age OR state that the study did not involve laboratory animals.*
Wild animals	*Provide details on animals observed in or captured in the field; report species, sex and age where possible. Describe how animals were caught and transported and what happened to captive animals after the study (if killed, explain why and describe method; if released, say where and when) OR state that the study did not involve wild animals.*
Field-collected samples	*For laboratory work with field-collected samples, describe all relevant parameters such as housing, maintenance, temperature, photoperiod and end-of-experiment protocol OR state that the study did not involve samples collected from the field.*
Ethics oversight	Ovine hearts from which transhydrogenase was purified were obtained from a local abattoir, hence no ethics approval was required.

Note that full information on the approval of the study protocol must also be provided in the manuscript.